Hypersonic Raindrops

J.E. Shepherd
Explosion Dynamics Laboratory
California Institute of Technology
Pasadena, CA

February 26, 2025

Raindrops keep fallin' on my head
But that doesn't mean my eyes
Will soon be turnin' red
Crying's not for me
'Cause I'm never gonna stop the rain
By complainin'
Because I'm free
Nothing's worryin' me

- Burt Bacharach and Hal David

1 Shocking Drops

The exquisite study of Dworzanczyk et al. (2025) on water drop impact (Fig. 1) by a hypersonic projectile reveals[1] short (< 1 μs), bright flashes of light recorded on high-speed cameras at the instant of impact. This observation prompts the question: What is the source of the luminosity? Bright flashes of light are often observed behind strong shock waves in gases, with a history of observation in shock tube studies (Keck et al., 1959, Gaydon and Hurle, 1963), and studies motivated by atmospheric explosions (Zel'dovich and Raizer, 1966). Bright flashes are also observed when bubbles collapse in water due to ultrasonic or flow-induced cavitation (Taylor and Jarman, 1970, Crum, 1994). However the drop impact events are more intricate, involving strong shock waves propagating in a multi-phase mixture of water (liquid and vapor) and air as well as in the liquid drop.

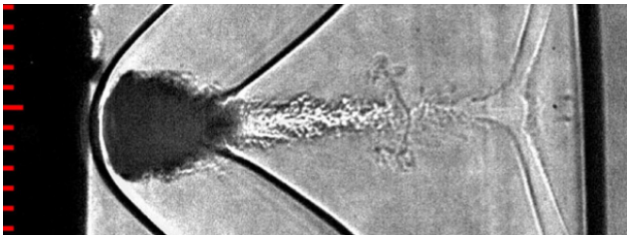

Figure 1: Close up of drop 3 at 14.75 μs, immediately before impact. Extracted from Supplement video of Dworzanczyk et al. (2025).

Luminosity of a hot gas or liquid is primarily a function of temperature although there are many other factors such as the composition, extent of the hot region, optical depth, collection optics, and wavelength sensitivity of the recording equipment. The goal of this short note is to consider some of these issues relevant to explaining the light flashes. Highly idealized, one-dimensional impact models are used to perform estimates of shocked states in gas and liquid, with an emphasis on estimating the maximum temperature of the two phases. A few ideas are presented about how to extend these considerations to include the multiphase, multidimenional characteristics of the impact event.

[1] Presentation by Parziale at Caltech, January 17, 2025 and video evidence in paper supplement.

2 Shock waves and thermodynamics

Consider a planar shock wave in a liquid. Given the shock speed, what is the postshock temperature? The corresponding question for a shock wave in a gas is addressed in a later section.

The classical approach developed by Walsh and Christian (1955) for solids and liquids is to use the shock jump conditions and thermodynamics to derive an expression for changes in temperature with volume along the shock adiabat. Approximating the thermodynamic properties for the liquid, the temperature equation can be integrated along the adiabat to obtain the temperature as a function of shock speed. The starting point is the shock jump conditions in the laboratory frame for a shock of speed U_s propagating into a stationary liquid at state (0) with a postshock state of (P, v, e) and speed u_p.

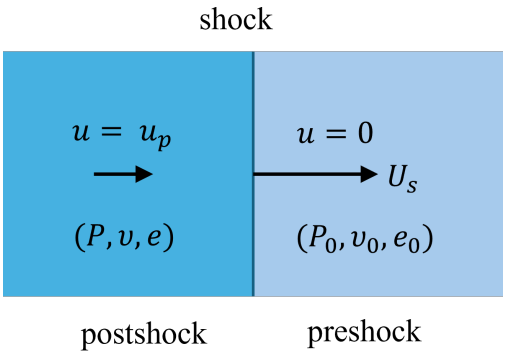

The model is the conventional treatment of a shock wave as a planar and thin, steadily-propagating discontinuity propagating in a material considered as a single-phase fluid. The shock jump conditions are an expression of the conservation or balance relationships. These can expressed in terms of specific volume $v = \rho^{-1}$, pressure P, and internal (thermodynamic) mass specific energy e using a control volume approach.
Mass balance:

$$u_p = U_s \left(1 - \frac{v}{v_0}\right), \tag{1}$$

Momentum balance

$$P = P_0 + \rho_0 U_s^2 \left(1 - \frac{v}{v_0}\right), \tag{2}$$

Energy balance

$$e + \frac{u_p^2}{2} = e_0 + P v_0 \left(1 - \frac{v}{v_0}\right). \tag{3}$$

By combining (1)-(3), a purely thermodynamic relationship for postshock properties, the Rankine-Hugoniot or shock adiabat equation is obtained,

$$e = e_0 + \frac{1}{2}\left(P + P_0\right)\left(v_0 - v\right). \tag{4}$$

The jump relationships are all functions of the nondimensional compression across the shock wave

$$1 - \frac{v}{v_0} = \frac{v_0 - v}{v_0},$$

which from (1) can be written in terms of the shock and particle speeds

$$\frac{v_0 - v}{v_0} = \frac{u_p}{U_s}.$$

As a consequence, to obtain solutions to the states downstream of the shock either the shock compression and shock speed, or the shock speed and particle velocity can be specified along with the initial states. Both approaches will be useful in our subsequent developments.

The next steps are to differentiate (4) and use the fundamental relation of thermodynamics to develop equations describing how temperature T and entropy s vary along the shock adiabat, following the approach of Walsh and Christian (1955). The fundamental relation of thermodynamics for a single-phase fluid is

$$\mathrm{d}e = T\mathrm{d}s - P\mathrm{d}\upsilon\,. \tag{5}$$

Combining (5) with (4), a relationship for entropy change along the shock adiabat is obtained,

$$T\mathrm{d}s = \frac{1}{2}\left(\upsilon_0 - \upsilon\right)\mathrm{d}P + \frac{1}{2}\left(P - P_0\right)\mathrm{d}\upsilon. \tag{6}$$

Evaluating all postshock properties on the shock adiabat $\mathcal{H}$, a differential equation for entropy is obtained,

$$T\left(\frac{\partial s}{\partial \upsilon}\right)_{\mathcal{H}} = \frac{1}{2}\left(\upsilon_0 - \upsilon\right)\left(\frac{\partial P}{\partial \upsilon}\right)_{\mathcal{H}} + \frac{1}{2}\left(P - P_0\right). \tag{7}$$

An equation for temperature can be found by considering $s(T,\upsilon)$ and the definition of the Grüniesen coefficient $\mathcal{G}$ and specific heat capacity at constant volume C_υ, an alternative expression for entropy change is obtained,

$$T\mathrm{d}s = C_\upsilon \mathrm{d}T + \frac{\mathcal{G}}{\upsilon}TC_\upsilon \mathrm{d}\upsilon. \tag{8}$$

Equating (7) and (8), a differential equation for temperature on the shock adiabat is obtained,

$$\left(\frac{\partial T}{\partial \upsilon}\right)_{\mathcal{H}} = \frac{1}{C_\upsilon}\left[\frac{1}{2}\left(\upsilon_0 - \upsilon\right)\left(\frac{\partial P}{\partial \upsilon}\right)_{\mathcal{H}} + \frac{1}{2}\left(P - P_0\right)\right] - T\frac{\mathcal{G}}{\upsilon}. \tag{9}$$

The pair (7) and (9) form a pair of ordinary differential equations for (s,T) as a function of υ on the shock adiabat if the properties

$$P, \quad C_\upsilon = \left(\frac{\partial e}{\partial T}\right)_\upsilon, \quad \mathcal{G} = \upsilon\left(\frac{\partial P}{\partial e}\right)_\upsilon, \quad \left(\frac{\partial P}{\partial \upsilon}\right)_{\mathcal{H}}.$$

are known or can be estimated on the shock adiabat. The pressure P and slope of the shock adiabat $\left(\frac{\partial P}{\partial \upsilon}\right)_{\mathcal{H}}$ can be obtained from the results of shock wave propagation tests as discussed in §4; the other parameters require additional considerations based on thermodynamic reasoning or statistical mechanics.

3 $U_s(u_p)$ relationship

A standard methodology in shock wave physics is to report the results of shock propagation measurements in terms of a relationship between shock speed U_S and particle (piston) speed u_p. The simplest form is just a linear relationship

$$U_s = a + bu_p, \tag{10}$$

where a and b are empirical parameters determined by shock impact experiments. Applicable to wide range of condensed materials, both liquids and solids above the elastic limit, extensive compilations of data and values of the parameters are available for many materials (Marsh, 1980). An elaboration of this method is to make the parameter b a function of the compression ratio. For example, one correlation used for water (Steinberg, 1987) has the form

$$U_s = a + u_p\left[b + c\left(\frac{u_p}{U_s}\right) + d\left(\frac{u_p}{U_s}\right)^2\right]. \tag{11}$$

An alternative expression is the "universal" Hugoniot for liquids proposed by Woolfolk et al. (1973)

$$\frac{U_s}{a_0} = 1.37 - 0.37\exp(-2u_p/a_0) + 1.62\frac{u_p}{a_0}, \tag{12}$$

where a_0 is the sound speed of the liquid at the initial state. The units for velocities are often given in km·s^{-1} equivalent to mm·μs^{-1} and pressures are specified in GPa (10^9 Pa). Older shock compression studies often report pressures as kbar or Mbar, 100 kbar = 10 GPa, 1 Mbar = 100 GPa.

Efforts to measure the $U_s(u_p)$ relationship for water begin the 1950s using high-explosive technology[2] (Walsh and Rice, 1957, Rice and Walsh, 1957), and later gas gun impact Lyzenga et al. (1982), Mitchell and Nellis (1982), Nagayama et al. (2002) and most recently, laser-driven shock waves Jeanloz et al. (2007), Millot et al. (2018). Selected data are compared with the two correlating functions in Fig. 2.

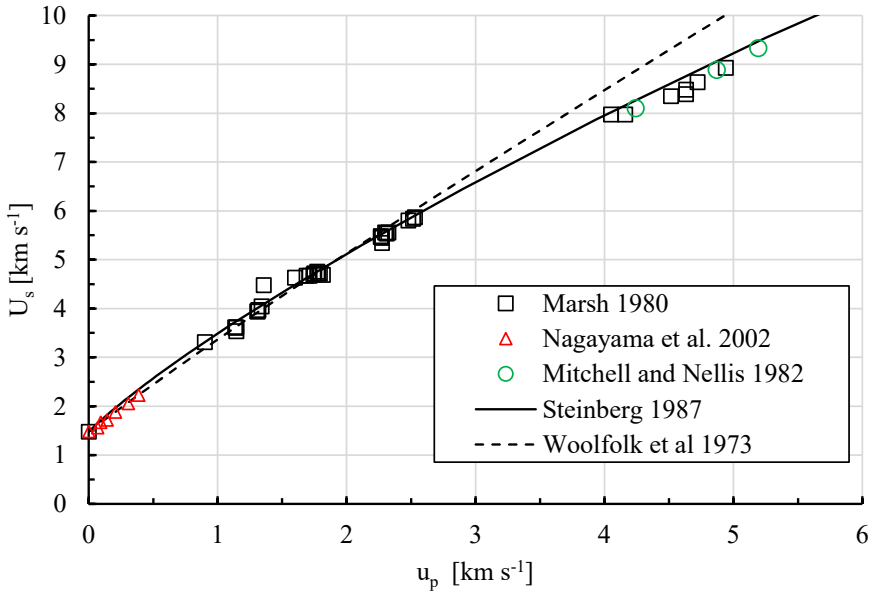

Figure 2: Selected data from shock wave propagation in water and two correlating functions.

4 $P(u_p)$ relationship

The $U_s(u_p)$ relationship can be used to compute shock pressure by combining (1) and (2)

$$P = P_0 + \rho_0 U_s u_p. \tag{13}$$

The relationship is exact and can be used either with measured U_s-u_p data or an analytic relationship $U_s(u_p)$ to determine a pressure-velocity $P(u_p)$ function, Fig. 3. The slope of the shock adiabat can be determined by differentiation of (1) and (13) to obtain

$$\left(\frac{\partial P}{\partial v}\right)_{\mathcal{H}} = -\rho_0^2 U_s^2 \frac{1 + \dfrac{u_p}{U_s}\dfrac{\mathrm{d}U_s}{\mathrm{d}u_p}}{1 - \dfrac{u_p}{U_s}\dfrac{\mathrm{d}U_s}{\mathrm{d}u_p}} \tag{14}$$

The formulation in terms of $P(u)$ is useful in graphical illustrations and quantitative solutions to one-dimensional wave interactions. By this method, a solution is obtained for pressure and velocity states associated with the propagating of waves resulting from planar impact and wave propagation through material interfaces. For example consider the situation described in Dworzanczyk et al. (2025), the impact of an water drop on an aluminum flyer plate with a relative velocity of 1500 m·s^{-1}. The drop surface is deformed into an oblate shape with an irregular front surface which is approximated as flat to apply the one-dimensional wave dynamics model of planar impact.

The treatment so far neglects another important aspect, the air between the drop and flyer plate with a strong shock wave in between, I will return to this aspect later. The purpose of this model is just to develop an estimate of the

[2]Contemporary with the early Los Alamos work were studies in the Soviet Union by Al'tshuler and colleagues, see the references in Bordzilovskii et al. and Kormer.

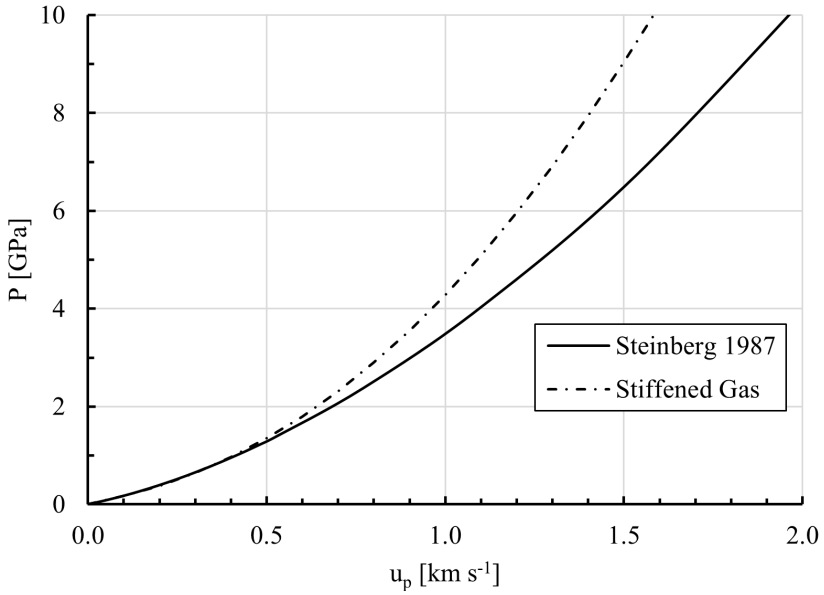

Figure 3: Pressure-particle velocity relationship for water based on the Steinberg fit to impact data of Fig. 2 and compared to the prediction of the Stiffened Gas model.

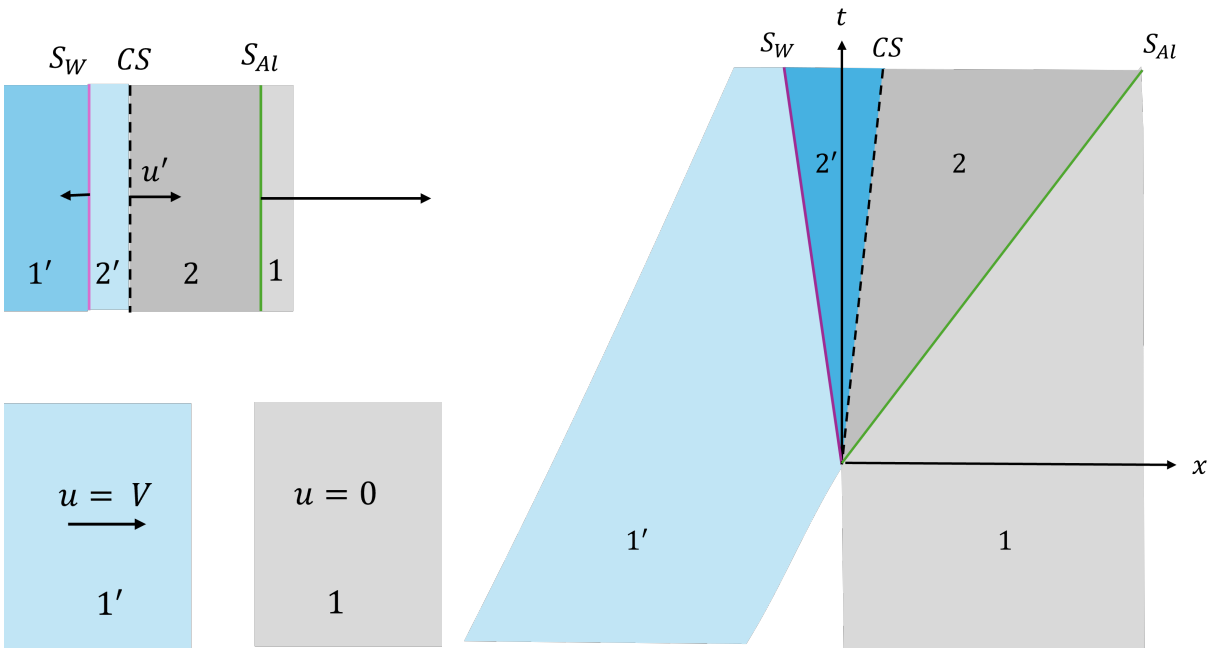

Figure 4: Model of initial wave propagation following planar impact

shocked water conditions following impact. This model is obviously unrealistic in details, but possibly useful to get a notion of the conditions immediately following the contact of the droplet and flyer plate. This approach is most relevant to the idealized gas gun testing used to obtain the U_s-u_p data or underwater explosion analyses (Shepherd, 1988). The impact between the drop and flyer plate will generate shock waves moving the opposite direction in the flyer S_{Al} (considered to be aluminium in our example) and in the water S_W. There are additional wave interactions at

the bounding surfaces which will play an important role following the initial impact.

The pressure and velocities at the water-flyer interface immediately after impact can be calculated by matching pressure $P' = P_2 = P_2'$ and velocity $u' = u_2 = u_2'$ at the contact surface (CS). An example of solutions for 4 representative impact speeds are shown in Fig. 5. The aluminum wave speed relationship was U_s = 5.35 + 1.34u_p (Marsh, 1980) and the water relationship was that of Steinberg (1987). In constructing these figures, the increase in water pressure due to the bow shocks, a maximum of 10 MPa, is neglected as this is less than 1% of the GPA pressures produced upon impact.

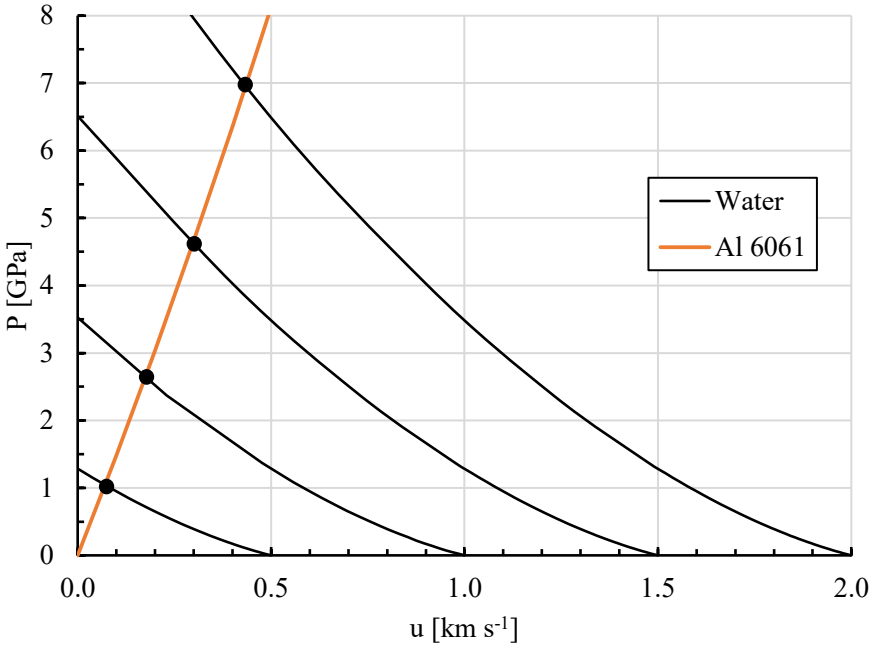

Figure 5: Graphical solutions to planar water impact on aluminum flyer for four impact speeds. The solutions for the shocked states are shown as the filled circles.

5 Water Temperature

Notable efforts to measure temperature behind shocks in water have used optical techniques; these include Kormer (1968), Lyzenga et al. (1982), Peng et al. (2011), Bordzilovskii et al. (2020). All of this data, reproduced in Figs. 24-26 in the Appendix A, has been collected at shock pressures greater than 30 GPa and the inferred temperatures were greater than 2000 K. Extrapolation of this data to lower shock pressures and temperatures is possible by using the predictive methods pioneered by Walsh and Christian (1955) for metals, extended to liquids by Rice and Walsh (1957), with further refinement by Cowperthwaite and Shaw (1970) and Peng et al. (2011).

Prediction of postshock temperature is sensitive to the assumptions about the thermodynamic properties, as discussed by Cowperthwaite and Shaw, when considered as a function of pressure, but relatively insensitive to the form of the $U_s(u_p)$ fitting function. The original approach of Walsh and Christian was to assume a constant value of $\mathcal{G}/v$ and C_v in order to integrate (9). In extending this approach to liquids, Rice and Walsh assumed that the parameter

$$\left(\frac{\partial h}{\partial v}\right)_P = \frac{C_P}{\left(\frac{\partial v}{\partial T}\right)_P} = \xi(P)$$

was only a function of pressure and evaluated this from shock reflection data (Walsh and Rice, 1957). Further, they assumed that C_P was a constant, 3.6 kJ·kg^{-1}·K^{-1}. Cowperthwaite and Shaw reconsidered the assumption the heat capacity was constant and explored the implication this was a function of temperature $C_v(T)$, approximating the variation to be identical to that of ideal gas values but keep $\mathcal{G}/v$ constant. However, it is unclear what value of heat capacity was used in their evaluation for water although Gurtman et al. (1971) indicates that they assume C_v = 3.26 kJ·kg^{-1}·K^{-1}. The model used by Shepherd (1988) followed the approach of Gurtman et al. (1971) which was based on an empirical correlations for $\mathcal{G}(v)$ and a constant value of the heat capacity, C_v = 3.365 kJ·kg^{-1}·K^{-1}. Gurtman et al. did an independent evaluation of the Walsh and Rice (1957) data using a thermodynamic model similar to that used for crystalline solids. They concluded that $C_v \approx$ 3.26 kJ·kg^{-1}·K^{-1} for $273 < T < 2500$ on the shock adiabat. Using the thermodynamic identity

$$C_P - C_v = T\left(\frac{\partial P}{\partial T}\right)_v \left(\frac{\partial v}{\partial T}\right)_P \tag{15}$$

they compute the difference between C_P and C_v at 2 GPa and find that it is on the order 0.35 kJ·kg^{-1}·K^{-1}. Given this rather modest difference, Gurtman et al. conclude that

> "Essentially, one could say that the choice of constant C_p (Rice and Walsh) or constant C_v (present formulation) affects the shape of the isentropes only as a correction term, and to a leading approximation the calculations are equivalent."

Peng et al. (2011) carried out an analysis using the Mie-Grüneisen approach with Hugoniot data as a reference and computed temperatures assuming specific heat C_v with a linear dependence on temperature and unstated assumptions about $\mathcal{G}(v)$. They concluded that C_v = 3.26 kJ·kg^{-1}·K^{-1} for $P < 51$ GPa and $T < 3340$ K.

These three predictions of temperature on the shock adiabat are shown in Fig. 6. For shock pressures less than 10 GPa, the temperature is approximately a linear function of pressure and the maximum deviation between the three methods is approximately 12%. At 10 GPa, the range of predicted temperatures is 732-843 K. The pressure and temperature of the water at the contact surface immediately after impact is given in Table 1 for the four representative flyer velocities considered in Fig. 5.

In order to improve on these estimates, the variation of heat capacity with both temperature and pressure, or equivalently volume, is required. To do so, consider computing internal energy by integrating along paths that account separately for changes in T and v. The thermodynamic identity

$$\left(\frac{\partial P}{\partial T}\right)_v = C_v \frac{\mathcal{G}}{v}, \tag{16}$$

transforms (5) and (8) to

$$\mathrm{d}e = C_v \mathrm{d}T + \left[T\left(\frac{\partial P}{\partial T}\right)_v - P\right]\mathrm{d}v. \tag{17}$$

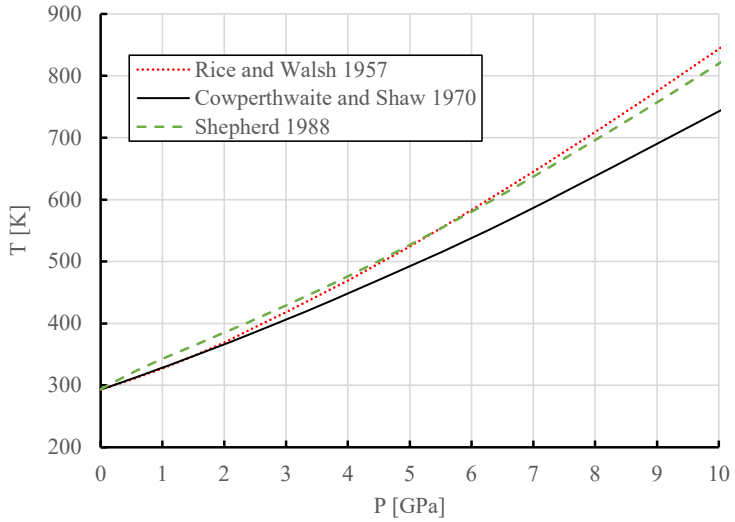

Figure 6: Estimated temperature of shocked water as a function of postshock pressure.

Table 1: Estimated postshock water pressure and temperature for the four representative planar impact cases.

V	P	T
km · s^{-1}	GPa	K
0.5	1.0	329
1.0	2.5	386
1.5	4.7	479
2.0	7.0	586

The second term vanishes for an ideal gas $Pv = RT$, which corresponds to the limit $v \to \infty$. This recovers the classical result the heat capacity of an ideal gas is only a function of temperature

$$\lim_{v\to\infty} C_v(T, v) = C_v^{ig}(T). \tag{18}$$

The specific heat of the ideal gas can be determined from statistical thermodynamics, the known molecular structure and spectroscopic measurements. The results (Fig. 7) can evaluated as a function of temperature from the polynomial fits of the NASA database McBride et al. (2002) using the Cantera software (Goodwin et al., 2017) package. The results can be interpreted in terms of effective degrees of freedom f and statistical thermodynamics, $C_v = f/2R$. At low temperatures, only translational and rotational degrees of freedom are active, $f = 6$. With increasing temperature, three vibrational modes become active and number of degrees of freedom approach the high-temperature limit of $f = 12$. The frozen (fr) solutions have a fixed composition of pure water. The equilibrium (eq) solutions consider dissociation to form a mixture of atoms and molecules, this is important for $T > 2500$ K at the pressures of interest.

To include the effect of molecular interactions using thermodynamics, integrate from an ideal gas state to the shocked state (T, v)

$$C_v(T, v) = C_v^{ig}(T) + \int_\infty^v \left(\frac{\partial C_v}{\partial v}\right)_T \mathrm{d}v'. \tag{19}$$

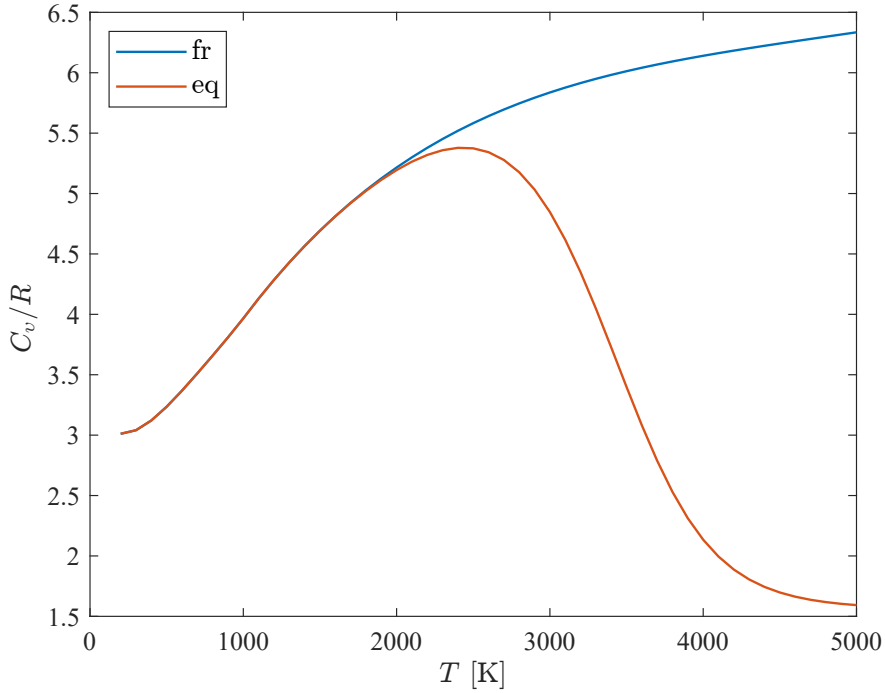

Figure 7: Nondimensional ideal gas specific heat capacity, C_v/R, as a function of temperature for H_2O(g) at 1 atm for frozen (fr) and equilibrium (eq) composition. For H_2O, $R = 0.461$ kJ·kg^{-1}·K^{-1}.

The variation of specific heat with volume at fixed temperature can be computed if state relation in the form $P(v, T)$ is known. From the definition of heat capacity

$$\left(\frac{\partial C_v}{\partial v}\right)_T = \frac{\partial}{\partial v}\left(\frac{\partial e}{\partial T}\right)_v, \tag{20}$$

interchanging derivatives

$$= \frac{\partial}{\partial T}\left(\frac{\partial e}{\partial v}\right)_T \tag{21}$$

and using (17)

$$= \frac{\partial}{\partial T}\left[T\left(\frac{\partial P}{\partial T}\right)_v - P\right], \tag{22}$$

I obtain

$$= T\left(\frac{\partial^2 P}{\partial T^2}\right)_v. \tag{23}$$

The evaluation of (19) can be performed using the ideal gas specific heat, an equation of state to compute the necessary derivatives, and numerical integration. The Cantera software provides this evaluation through an implementation of the water equation of state described in Reynolds (1979). This equation of state was developed for analyzing and design of powerplants using steam (Keenan et al., 1969) and is limited in range of temperatures < 1500 K, and pressures < 100 MPa. Unfortunately, as shown in Fig. 8, this precludes computing temperature on the shock adiabat except for the very weakest waves. However, these results can be used to evaluate some trends of how volume and phase change influence the specific heat values.

For temperatures greater than the critical point, $T_{cp} = 647.3$ K, the integration (19) is straight forward and only limited by the availability of a reliable equation of state that covers the compressed fluid states. The general trend at

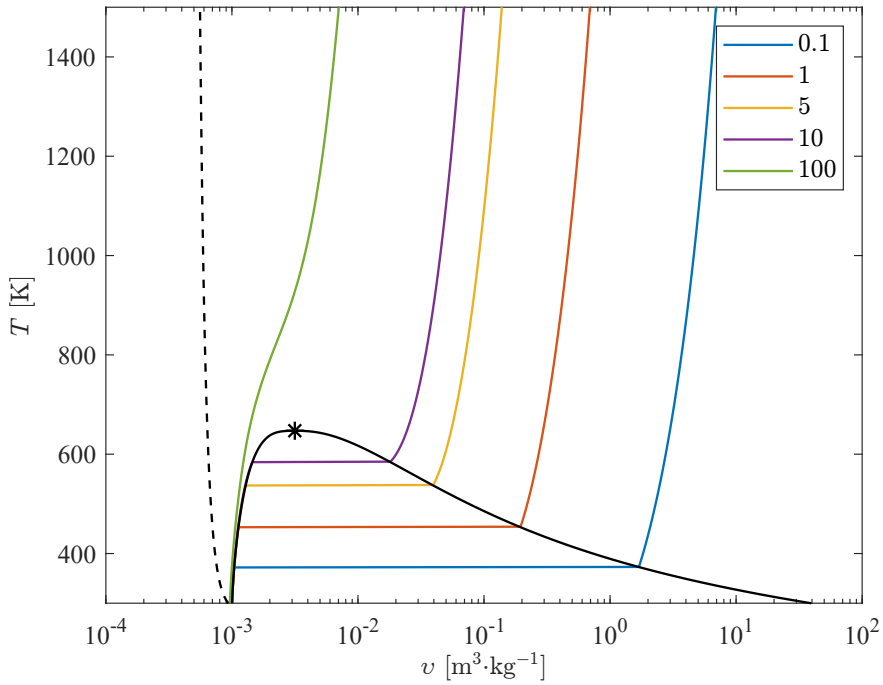

Figure 8: Water equation of state in $T - v$ coordinates illustrating the saturation boundary (solid lines), critical point (*), selected isobars (legend is P in MPa), and the estimated $T(v)$ locus on the shock adiabat (dashed line).

low temperatures is an increase in specific heat capacity with decreasing volume, Fig. 9; the nonmonotonic behavior and decrease in the departure for higher temperatures is due to inflection points in the isochores. It is unclear if the rapid variation at the smallest volumes is realistic. The equation of state implemented in Cantera is not applicable to the highly compressed fluid states, as can be seen by the separation of the P = 100 MPa isobar from the estimated postshock temperature on Fig. 8. As a consequence, the results cannot be used to validate the heat capacity values used in the Rice and Walsh approach.

For subcritical shock temperatures, the change in heat capacity through the phase change is discontinuous and has to be separately computed using thermodynamic data. This step is important for weaker shocks, $P \leq$ 5-8 GPa, which are estimated to have subcritical temperature states. This effect is illustrated in Fig. 10 using the specific heat capacity for liquid and vapor saturated states. The effect of the molecular interactions is to increase the specific heat with decreasing volume at a given temperature. This effect creates the substantial difference shown between the saturated vapor and ideal gas values. The order of magnitude of peak heat capacities in the saturated liquid are comparable to the value C_v/R = 7 used to compute Fig 6. Additional thermodynamic considerations about the water equation of state are given in the Appendix B.

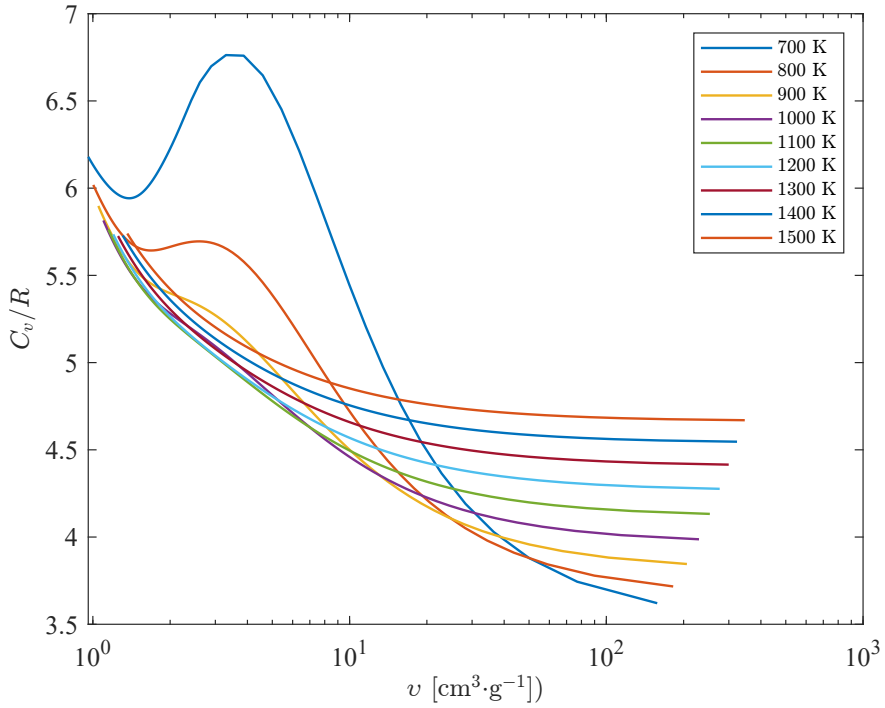

Figure 9: Nondimensional specific heat capacity of water on selected supercritical isotherms as a function of specific volume. The lower limit of υ on each isotherm is determined by upper limit on pressure of 1000 MPa. The upper limit of υ is determined by taking an arbitrary lower limit on pressure of 1 kPa. computed using the NIST implementation of Wagner and Pruß (2002)

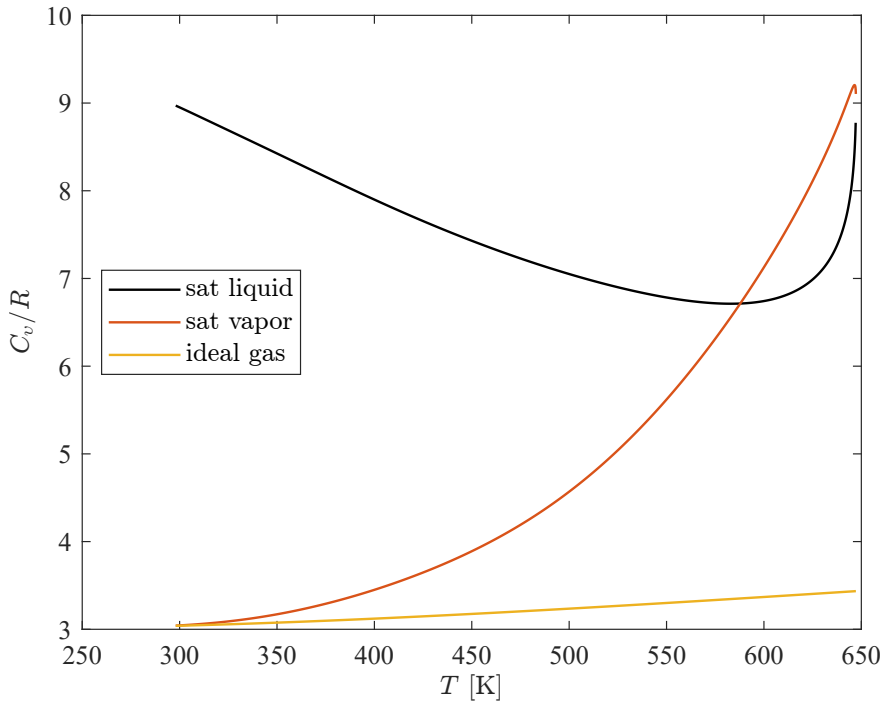

Figure 10: Nondimensional specific heat capacity of water at constant volume for saturated liquid, vapor and ideal gas state as a function of temperature. The behavior in the vicinity of the critical point is not correctly described by the usual engineering equations of state (Thompson, 1978), hence the gap in the curves.

6 The Stiffened Gas Equation of State

The simulations in Dworzanczyk et al. are sophisticated and impressive in predictive ability for the drop surface dynamics. The drop-flyer impact is not considered in these computations but it is useful to consider the extension to impact and the possibility of predicting temperature with this approach. A major drawback to extending their approach to determine temperature is that the water equation of state used is of the form $P(e, \rho)$. This is a widely used approach in hydrodynamic situations, e.g., compressible flow modeling based on a conservative form of the Euler equations. However, this is an incomplete equation of state and additional considerations are needed to compute $T(e, \rho)$. Further, the particular equation of state chosen by Dworzanczyk et al. to model each phase (water and gas) is the *stiffened gas* equation of state in the form

$$P = (\gamma - 1)\rho e - \gamma P^{\infty} \tag{24}$$

where γ and P^{∞} are empirical parameters chosen to match selected properties of the phase.

This equation is exact for the perfect gases with $P^{\infty} = 0$ and γ is the usual adiabatic exponent. However, for high temperature gases with dissociation and ionization this is not valid and the ideal gas relationship must be used to compute P

$$P = \rho R T, \quad R = \frac{\mathcal{R}}{\mathcal{W}}. \tag{25}$$

The mean molar mass $\mathcal{W}$ depends on the composition; constant at low temperatures and a function of (T, P) at high temperatures for gases in equilibrium.

The dependence $P(\rho, e)$ complicates the computation of high-temperature gas motion, so-called conservative methods of computing compressible flow evolve $(\rho, \mathbf{u}, e)$ and require a relationship $P(\rho, e)$ in order to compute the pressure derivatives that are needed to update the momentum equations. The computation of temperature is straightforward only as long as $e(T)$ is a monotonic function independent of ρ or equivalently P. As shown in Fig. 11 for the curve (fr), this model is appropriate only for temperatures less than 2500 K. At higher temperatures $e(T, P)$ for equilibrium states, shown as the isobar curves labeled with P in Fig. 11. Efficient methods for computation in this regime include using interpolation of tabulations (SESAME) or functional relationships fit to equilibrium computations (Tannehill and Mugge, 1974). For unsteady flows for which it is important to resolve the processes at the molecular level using reactive version of the conservation equations with chemical and molecular (vibrational) relaxation processes modeled using rate equations.

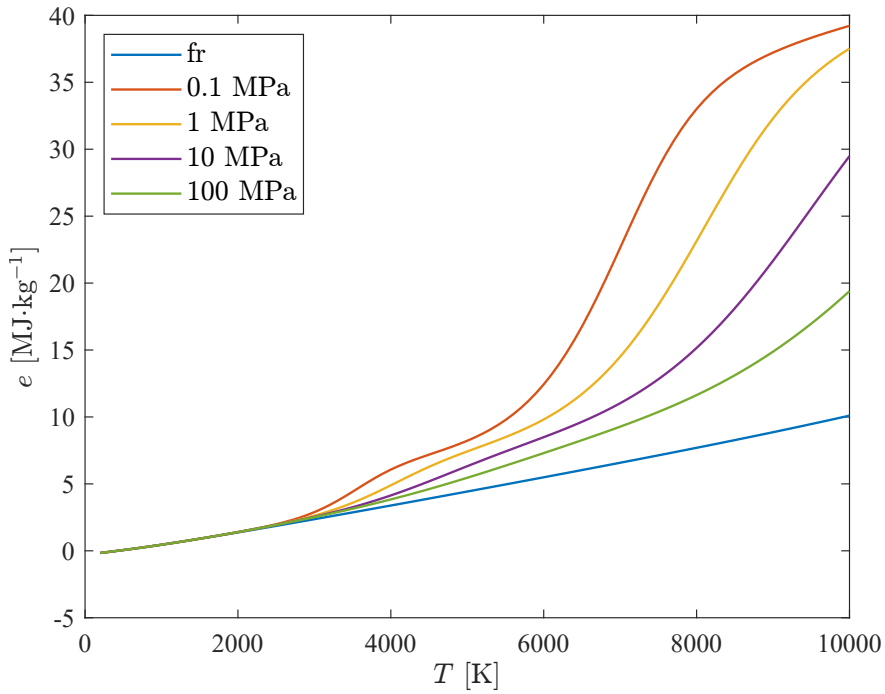

Figure 11: Internal energy of hot air for frozen (fr) and equilibrium states (labeled by pressure).

The construction of a liquid water equation of state that spans the regimes between weak (acoustic waves) and strong shock waves is more challenging than for ideal gases. The stiffened gas model is widely used (e.g. Johnsen and Colonius, 2008), for weak shock waves in water, $u_p \ll 500$ m·s^{-1} but becomes increasingly inaccurate for stronger shocks. It is possible to obtain an analytic solution (Appendix C) for the $U_s(u_p)$ relation for the stiffened-gas equation of state. A useful choice of the parameters is to fit the intercept and slope of $U_s(u_p)$ at $u_p = 0$ to obtain γ = 6.58 and P^∞ = 334 MPa. As discussed in Appendix C, this ensures that small amplitude motions are isentropic. Comparisons with the impact data are shown Fig. 12 show the increasing deviation from the data with increasing impact velocity. The stiffened gas model has its origin in modeling isentropic compression of water by Harlow and Amsden (1971) which is appropriate for weak shock waves that generate only small entropy changes. Consistent with the evaluation by Cocchi et al., reasonable agreement with the data is obtained for $u_p \leq 500$ m·s^{-1}. For larger impact speeds, up to 2000 m·s^{-1}, a linear correlation or the Woolfolk et al. (1973) model are both acceptable fits to the data.

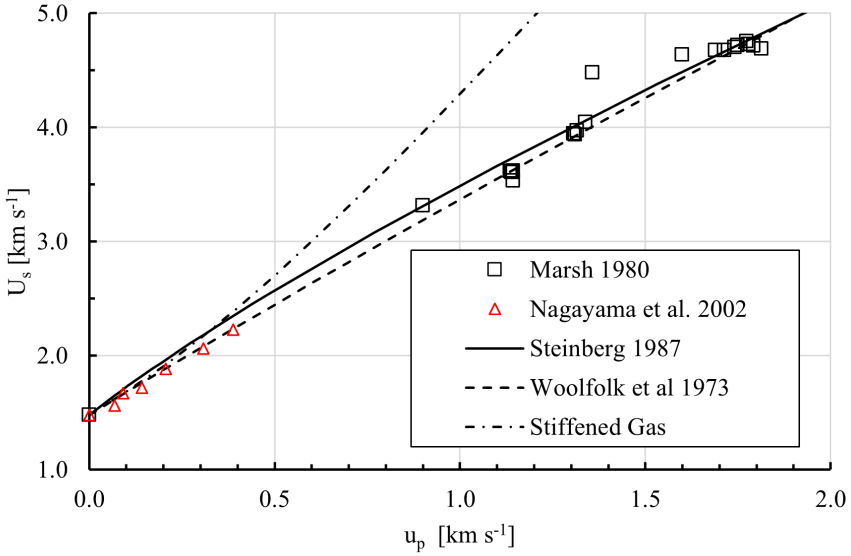

Figure 12: Comparison of stiffened gas model for liquid water to impact data, a linear fit (U_s = 1481.63 + 1.8907u_p), and the model of Woolfolk et al. (1973).

7 Shocked gas temperature

Based on the observations, Dworzanczyk et al. (2025) deduced the schematic flow field shown Fig. 13. The configuration is of a slightly curved bow shock (between states 0 and 1) ahead of the flyer plate with the initially stationary drop penetrating the shock deformed and surrounded by a layer of mist stripped from the surface. The drop is accelerated by the flow behind the flyer shock but decelerated by the highly curved bow shock (between states 2 and 3) ahead of the drop. For the purposes of estimation, the considerations of Dworzanczyk et al. suggest the relative velocity between the shock and flyer is comparable to the flyer velocity. The flow behind the bow shocks is nonuniform due to the flow slowing from the shock front to the flyer and drop surfaces. Dworzanczyk et al. propose a simple mode of the stagnation process and show that along the centerline the variation in thermodynamic state between the shock front and stagnation is modest. Neglect this variation, state 3 is assumed to be equal to state 2 for the present purposes.

The temperatures behind the shocked gas can be determined by using realistic model of the gas thermochemistry McBride et al. (2002), the Cantera software Goodwin et al. (2017), and the Shock and Detonation Toolbox EDL (2019). Estimated temperatures in front of the flyer plate and the droplet are much higher than the temperatures estimated for water due to the large extent of the compression, a factor of approximately six, and the lower specific heat capacity in the gas as compared to the liquid. The temperature and pressure of state 2 are higher than state 1 because the shock wave ahead of the drop is propagating into the compressed, elevated temperature gas that was processed by the flyer shock. State 4 corresponds to the state created by the reflection of the drop bow shock from the flyer plate, just before

the drop itself reaches the flyer.

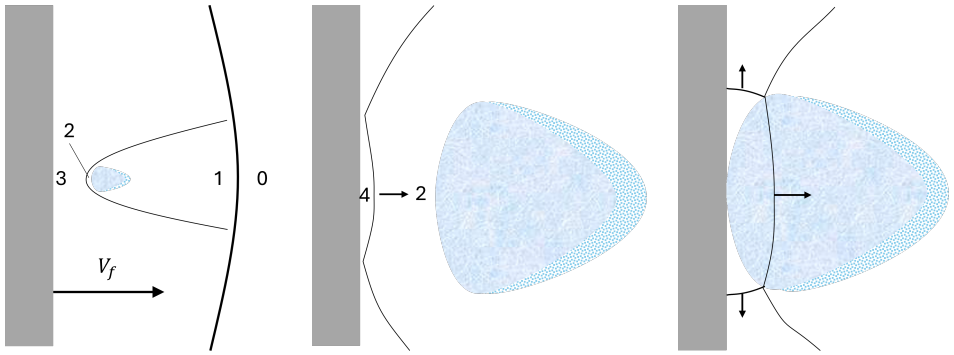

Figure 13: (a) Schematic of shock waves in air before bow shock and drop impact event based on observations of Dworzanczyk et al. (2025). (b) proposed configuration of reflected bow shock before drop impact, regular reflection. (c) transition to Mach reflection.

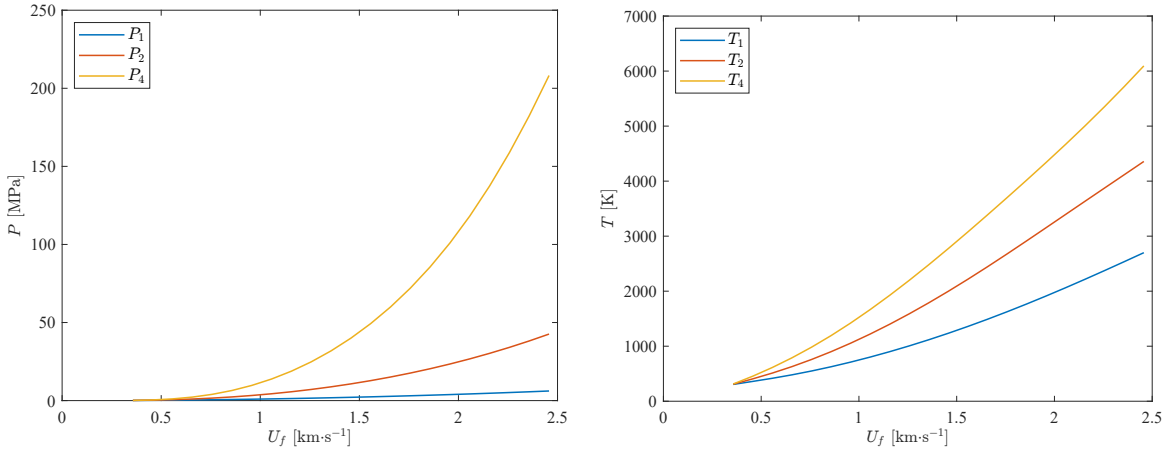

Figure 14: Postshock conditions for flyer shock (state 1), drop shock (state 2), reflected drop shock (state 4) computed using equilibrium dry, air at nominal conditions of 20°C and 1 atm. (a) pressure, (b) temperature.

The estimated pressures behind the gas shocks, Fig. 1a, are 10^{-3} of the liquid water pressures predicted for the ideal impact, Fig. 5. From (13), this is clearly due to the air density being 10^{-3} of the liquid water density although the flow speeds behind an air shock are much higher than a water shock for the same shock speed, Fig. 16. The postshock temperatures are a factor of four to five higher than the peak shock temperature estimated for the water at an impact speed of 2 km·s^{-1}. The highest gas temperatures are produced in state 4 when the bow shock reflects from the flyer. This shock may reverberate between the flyer and drop, resulting in additional compression states with even higher pressure and temperature.

The estimated species concentrations (shown as mole fractions) for the major species are shown in Fig. 15 for state 4 created following reflection of the bow shock from the flyer. The computations were performed with and without ions and electrons. The only significant ionized species is NO^+, with a mole fraction of 2×10^{-5} (not shown in the figures) at the highest temperatures. The high pressures behind the shock waves suppresses dissociation and ionization to a much greater extent than for observed in low pressure shock tube testing; a consequence of the Le Chatelier's principle. With increasing temperature, the reactions between O_2 and N_2 create NO and the thermal dissociation for O_2 create atomic oxygen O. Significant amounts of dissociation in state 4 do not occur until $U_f > 1.5$ km·s^{-1} corresponding to $T > 3000$ K.

The estimates of temperatures and species given in this section assume very rapid equilibration behind the shock waves. The process of equilibration does not take place instantaneously but over a finite duration determined by the processes of physical and chemical reaction. This can be accounted for by using a network of reactions and associated reaction rates to account for the finite rates of vibrational-translational energy exchange and chemical reaction. We anticipate that these processes will be relatively rapid given the high pressures and temperatures in states 2 and 4.

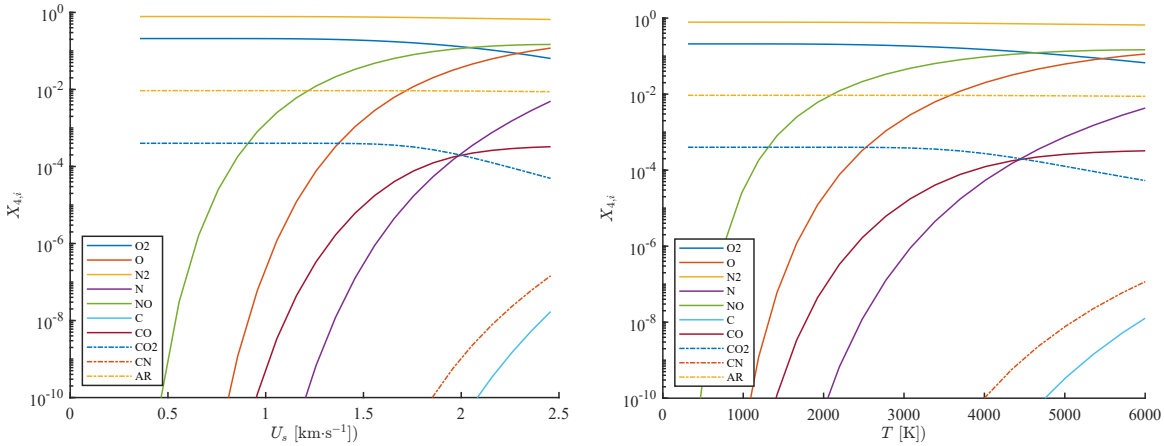

(a) (b)

Figure 15: Postshock mole fractions of major species for reflected drop shock (state 4) computed using equilibrium. Shown as a function of (a) flyer speed and (b) postshock temperature.

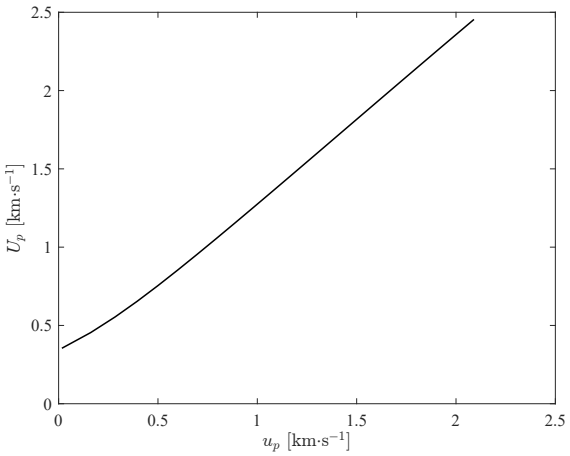

Figure 16: Shock speed as a function of particle velocity for shock waves into equilibrium dry, air at nominal conditions of 20°C and 1 atm.

8 Drop Impact

An example impact event is illustrated in Fig. 17 which shows four frames from the shadowgraph images for drop 3 of Dworzanczyk et al., a 1.87 mm initial diameter drop impacted by a 1469 m·s^{-1} flyer plate. The actual impact is estimated to occur at 15.6 μs, just after Fig. 17b. Successive frames are 250 ns apart and acquired with a 100 ns exposure. An apparent flash of light is observed as a bright region close to the drop impact location on the flyer plate on Fig. 17c, a dimmer region is observed near that location on the next frame, Fig. 17d. A more quantitative representation is obtained by extracting the gray scale values[3] (presumably proportional to the integrated light intensity I on the camera sensor) along a line passing normally through the impact location, Fig. 18. Comparing the pre- and post-impact images, the bright feature can be observed in Fig. 18d as an increase in I from the value of 0.2-0.3 corresponding to the drop shadow to peak value of 0.7-0.8 in the region 6 , $X < 7$, and $18 < y < 21$ mm. The normal portion of the bow shock ahead of the drop is visible at 4 mm on Fig. 18b and the oblique portions are visible at 15 and 23 mm on Fig. 18d. For reference, the background illumination level is on the order of $I \sim 0.8$ and the drop shadow (before impact) $I \sim 0.2$. The peak I of the bright region is about 0.8, 2-4 times the shadow. Significant postprocessing was carried out on the original images in order clean up artifacts (ghosting), flatten the background, and improve the contrast. Examination of the original digital output of the camera reveals that the relative signal level corresponding to the bright regions is much lower on the original than on the processed images.

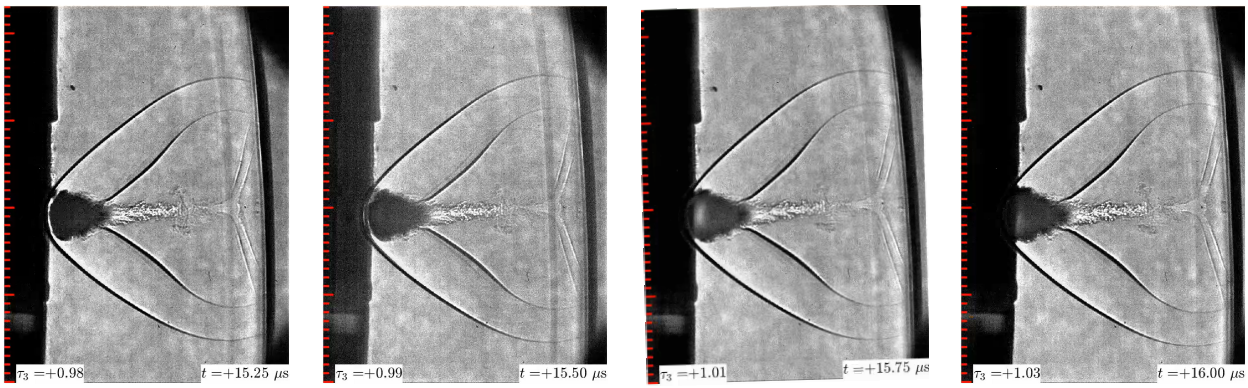

(a) (b) (c) (d)

Figure 17: Sequence of successive frames bracketing the impact event for drop 3 of Dworzanczyk et al. (2025). (extracted from Supplement video).

If these bright regions are indeed due to the self-luminosity, these regions would have to be quite bright to be recorded on the camera sensor as there was a bandpass filter used in front of the camera to limit the contamination of the image due to the muzzle flash. Further investigation is also required to rule out the possibility that the bright region on the image is an artifact resulting from transmission of the laser backlight through the shocked drop leading edge region, or reflection from the flyer surface followed by refraction through the liquid. The drop bow shock relfections could vaporize the mist and create a transparent gas layer. These possibilities could be ruled out through additional testing and modeling. The refraction effect of the shadowgraph system is important to consider when interpreting the images, this is evidenced by the characteristic appearance of the shock waves as dark and light bands associated with the caustics and created by refraction in the high density gradient within the shock front.

Brightness of a luminous region is associated with the emission (spontaneous and stimulated) of photons due to transitions between atomic and molecular energy levels[4] of the electronic quantum states. The magnitude of the photon emission depends on the population of the states, the density of the emitters, and the transmission of the photons through the emitting and surround regions. Light collected and recorded on a sensor produces electrical signals that proportional to flux of photons intercepted by the imaging optics integrated over the recording time of the sensor electronics. Not all wavelengths of light emitted will be recorded, this will be determined by the spectral sensitivity of the sensor and the spectral transmission function of the imaging optics taking into account such details of each optical

[3]The images in the MP4 format videos are given in RGB format with 8-bit values, these were converted to gray scale values and scaled by the maximum level of 255. The video images will be degraded compared to the raw gray-scale, uncompressed images directly from the camera sensor.

[4]In ionized gases with significant electron densities, the capture or acceleration of electrons will also contribute to emission.

element including coatings as well as materials.

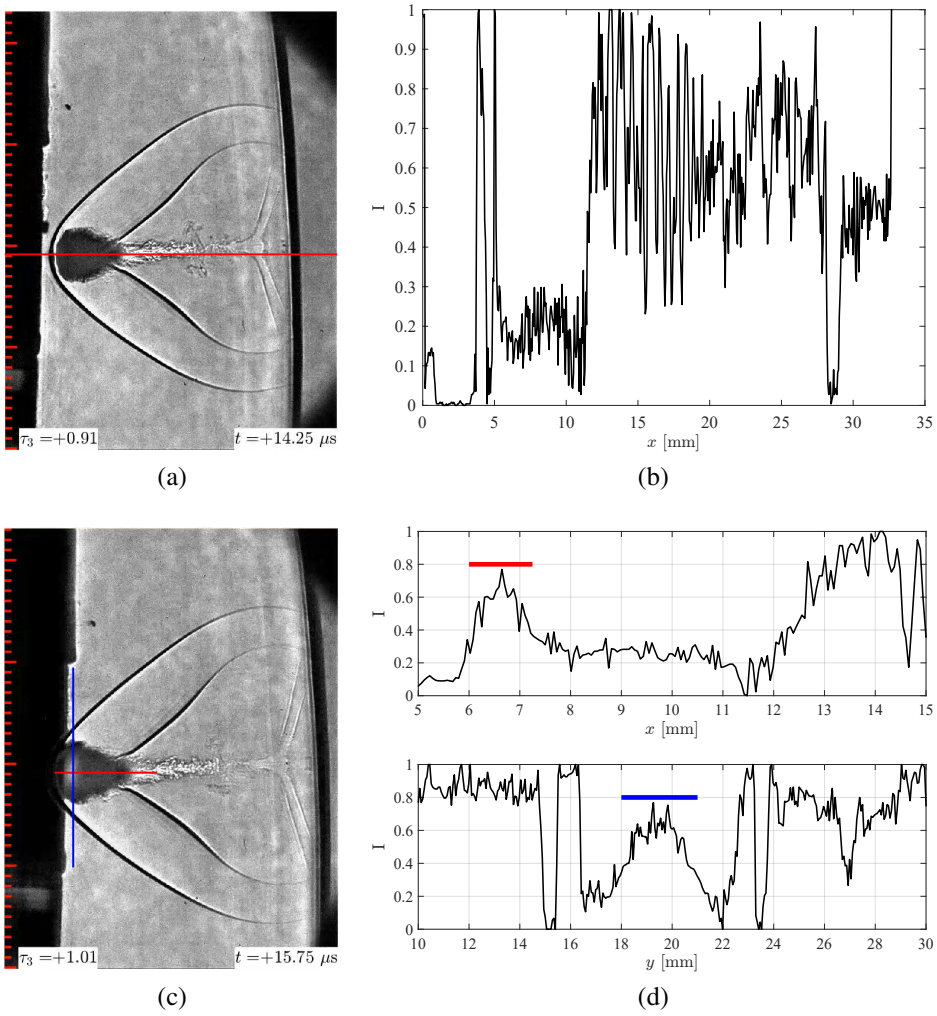

Figure 18: Two images and extracted normalized gray scale values I, along a lines extending through the impact point and bright feature. (a) and (b) are for frame 60 taken 1.35 μ s prior to impact. Line data is perpendicular through impact point. (c) and (d) are for frame 66, taken about 1.15 μs after impact. A more limited range of data are extracted along horizontal (red) and vertical lines (blues) through the bright feature which is demarcated by the color bars spanning the extent. Extracted from Supplemental video of Dworzanczyk et al. (2025).

Accepting that the images do indeed show light emission, how can very bright regions of luminosity be produced during the impact? A plausible explanation is that shock heating generates high temperatures to populate the excited states and create a dense, luminous region. To go further with this possibility we need to determine What temperatures would be needed to create significant emission and estimate the number of photons incident on the camera sensor.

8.1 Emission Brightness

The brightness of a hot gas or liquid will depend primarily on the thermodynamic temperature of the material and range of wavelengths that are being observed. From a molecular and atomic point of view, emission of water at temperatures less than 3000 K is in the infrared region due to transitions between vibrational states of the ground electronic state. Air at these conditions and high pressure behind shock waves is primarily composed of molecular N_2 and O_2 which do not radiate or absorb in the IR. To obtain significant brightness in the visible region (400-800 nm) much higher temperatures, T $>$ 7500 K, are needed to create sufficient populations to enable vibrational-rotational

transitions between electronic states as well as individual spectral lines of electronic transitions in atoms, (see Ch. II and V of Zel'dovich and Raizer, 1966).

Air

The experience with air in shock tubes (Gaydon and Hurle, 1963) is that for temperatures less than 3000 K is that the main contribution to brightness in the visible region for air and water vapor is due to contamination, with band radiation form CN, and C_2, and line radiation from Na, K, Fe, and Al metals and oxides. Diaphragm material (plastics and aluminum) and contamination can also contribute substantial broadband background. Absorption and emission coefficients (Kirchhoff's relation shows the two are identical in thermal equilibrium) depend strongly on the density as well as temperature. Entry into the atmosphere and radiation from rocket exhaust have motivated a large number of shock tube studies beginning in the 1950s (Keck et al., 1959) and continuing to the present. To achieve high temperatures, the nature of shock tube technology requires working at very low density to obtain high temperatures (Fujita et al., 2002); as a consequence the results are not directly applicable to the present situation. For example, state 4 behind the reflected bow shock shown in Fig. 13 has an estimated temperature of 2900 K, a pressure of 45 MPa, density of 54 kg·m^{-3}. These densities are 10^3 to 10^5 times those typically obtained in chemical physics shock tube studies. Similar conditions have been examined in connection with shock waves created by nuclear weapons (Churchill et al., 1966, Armstrong et al., 1965) and high-enthalpy shock tunnels used for hypersonic flight research (Parekh et al., 2018). At sufficiently high temperatures, ionization of Ar (argon) and NO (nitric oxide) are important and electron interactions with these ions will contribution to the luminosity. Neutral NO has strong radiation in the UV with a band at 210-250 nm.

Water

The water molecule has three vibrational modes at fundamental frequencies ν_1 = 3657 cm^{-1} (symmetric stretch), ν_2 = 1595 cm^{-1} (bending mode), ν_3 = 3756 cm^{-1} (antisymmetric Stretch). The ν_1 and ν_3 vibrational-rotational fundamental modes contribute to form the band spectrum at centered at 2.7 μm and the ν_2 vibrational-rotational fundamental mode form the band spectrum centered at 6.3 μm. Combination and overtone ($\Delta\nu > 1$) transitions result in bands at shorter wavelengths and there is a substantial rotational spectrum at longer wave lengths. Extensive spectroscopic studies in gaseous water using emission and absorption have been carried out in shock tube studies (Parker et al., 1996), burners (Ludwig, 1971, Coppalle and Vervisch, 1986) to reach temperatures up to 3000 K, and the HiTEMP database for H_2O (Rothman et al., 2010) is considered reliable up to temperatures of 4000 K. At sufficiently high temperatures, substantial quantities of OH (hydroxyl radical) can be formed and will contribute radiation in the UV with a strong band around 300-320 nm. Data for liquid water in the visible is scarce as the absorption coefficients are so low and in the infrared because the absorption coefficients are so large. The experimental data on liquid water emission under impact presented in Appendix A is at much higher impact velocities than the range of interest for the study of Dworzanczyk et al..

Brightness

To quantify brightness of the emission, we need briefly consider the generation and transport of radiation in the hot material. The simplest ideas about emission are to consider thermal equilibrium and emission from a plane layer of thickness ℓ. The emission can be quantified as the spectral radiance L_λ in the direction normal to the layer; L_λ has units of power per steradian and unit wavelength, a convention choice of units is W·m^{-2}·sr^{-1}·nm^{-1}. The emission is proportional to radiance of blackbody radiation, the Planck function B_λ, corrected for the transparency of the layer and stimulated emission.

$$B_\lambda = \frac{2hc^2}{\lambda^5} \frac{1}{e^{\frac{hc}{\lambda k_B T}} - 1} \tag{26}$$

The solution to the radiative transfer equation (p. 135, Vol. 1 Zel'dovich and Raizer, 1966) for the spectral radiance at the surface of the slab with constant temperature T and spectral absorption coefficient κ_λ is

$$L_\lambda = B_\lambda(T) \left(1 - e^{-\tau_\lambda}\right), \tag{27}$$

where the optical depth is defined by the integral through the depth of the slab

$$\tau_\lambda = \int_o^\ell \kappa'_\lambda \, \mathrm{d}s, \tag{28}$$

where the spectral absorption cofficient corrected for stimulated emission is

$$\kappa'_\lambda = \kappa_\lambda \left(1 - e^{-\frac{hc}{\lambda k_B T}}\right). \tag{29}$$

At visible wavelengths and high temperatures, this correction is negligible and the approximation $\kappa'_\lambda \approx \kappa_\lambda$ is often used

The spectral absorption coefficient is a function of wavelength, gas composition, temperature and pressure. There are two limiting cases, optically thick $\tau'_\lambda >> 1$ for which

$$L_\lambda \approx B_\lambda(T) \tag{30}$$

and the optically-thin case of $\tau'_\lambda << 1$, for which

$$L_\lambda \approx \tau'_\lambda B_\lambda(T) \tag{31}$$

A common approximation for high-temperature gases is to neglect the correction due to stimulated emission and considering a uniform composition and temperature, we obtain the optically thin approximation for emission

$$L_\lambda \approx \ell \kappa_\lambda B_\lambda(T). \tag{32}$$

This highly idealized representation neglects some important features of the actual event, more notably that scattering from the mist surrounding the drop, refraction and reflection within the liquid drop, the actual geometry is certainly not a slab, and the shadowgraph laser back illumination may penetrate through the shocked drop and mist. However idealized these models, they do illustrate the essential roles of absorption coefficient, depth of the radiating material, and temperature.

The spectral radiance of blackbody emission is illustrated in Fig. 19a for some representative temperatures for the visible and mid-IR spectral range. The effect of the sensor response and the narrow band filter is evaluated by integrating the Planck function assuming unity response over the wavelength window, Fig. 19b. Unity response is appropriate for the narrow band filter but less so for entire visible spectrum given the reported variations in camera spectral sensitivity Crooks et al. (2013a). What the results in Fig. 19b show is that the radiance transmitted through the narrow band filter will be on the order of 1/25 of the radiance through the entire visible spectrum. Although decreasing the number of photons on the sensor, there may still be enough light to record an image. The peak in the blackbody spectral radiance is given by Wein's displacement law, λ_{max} = 2898/T , λ in μm and T in K. At 3000 K, λ_{max} is 966 nm, outside the spectral range of the camera although there is a significant contribution to the radiance over the range 400-800 nm.

Absorption Coefficients

A detailed calculation of absorption for high-temperature, equilibrium air was carried out by Churchill et al. (1966) as a function of air density and temperature. This appears to be one of only public data sets with thermodynamic states close to the conditions of interest for this study. The data are tabulated in Armstrong et al. (1965) up to 10 kg·m^{-3} and 24000 K. The absorption coefficient is shown in Fig. 20a for 3000 K and 12.93 kg·m^{-3}. For a wavelength of 620 nm, close to the range of the laser line filter, we have extrapolated results up to 100 kg·m^{-3} using a quadratic function in logarithmic coordinates, Fig. 20b. By the way of a verification, the model of Churchill et al. (1966) is compared to the experimental data of Keck et al. (1959) at 8000 K in Fig. 21a. This comparison is slightly flawed as the Churchill et al. absorption coefficients were not interpolated to same density as the Keck experiments but were about 30% higher. Unfortunately, no data could be found at lower temperatures for validation tests. Finally, an estimation of the spectral radiance of equilibrium air at 3000 K was performed using 12.9 kg·m^{-3} model of Churchill et al. (1966) and the density extrapolation shown in Fig. 20b was used to estimate the spectral radiance at 3000 K and 50 kg·m^{-3}, both for a depth ℓ = 4 mm.

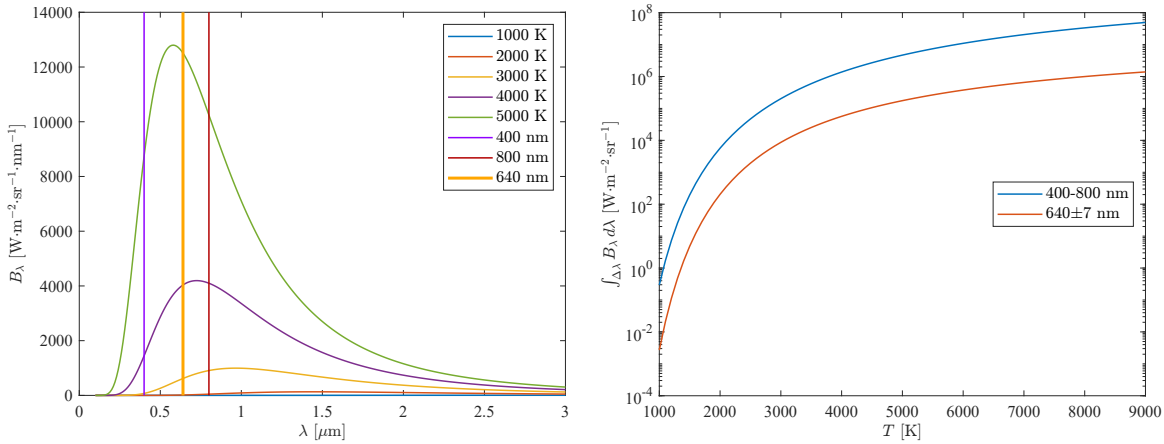

(a) (b)

Figure 19: (a) Spectral radiance of blackbody (Planck) radiation. (b) Wavelength integrated spectral radiance for visible range (400-800 nm) and for a narrow band (640 $\pm$ 7 nm) at the illuminating laser wavelength.

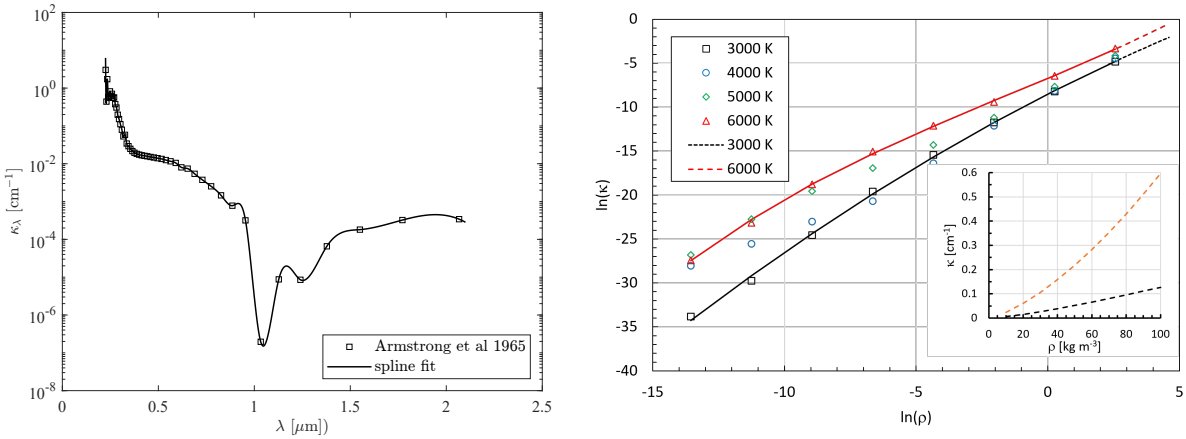

(a) (b)

Figure 20: (a) spectral absorption coefficient for air at 3000 K and 12.93 kg·m^{-3}. (b) Data and extrapolation of the spectral absorption (cm^{-1}) at 620 nm as a function of density (kg·m^{-3}). Based on data of Armstrong et al. (1965).

Are there enough photons?

In order to evaluate if the emission was sufficiently bright to be recorded on the camera sensor, we need to estimate the number of electrons N_e^- that will collected during the integration time t_{int} of each frame. The number of electrons are equal to the quantum efficiency η times the number of photons N_{hv}. The radiance L_i imaged on a sensor pixel of area A_i is equal to the radiance L_o collected by the imaging system if we neglect the losses in the imaging optics. The total number of photons incident on a pixel will be equal to

$$N_{hv} = A_o \Omega_o \frac{\int_0^{t_{exp}} L_o(t) \mathrm{d}t}{h\nu}, \quad L_o = \int_{\lambda_1}^{\lambda_2} L_{o,\lambda} \mathrm{d}\lambda. \tag{33}$$

where $[\lambda_1 \lambda_2]$ is the effective wavelength range passed through the imaging optics, in this case the bandwidth of the laser line filter. The convention in sensor technology is that the quantum efficiency is based on the total area of the pixel which will include the on-chip electronics. The actual sensitive element will occupy a smaller fraction of the that area, the ratio of sensitive to total area is known as the fill factor. The solid angle Ω_o of light collected by a remote imaging system with a effective light gathering diameter of $2r$ at distance R from the source subtends a half-angle θ_0

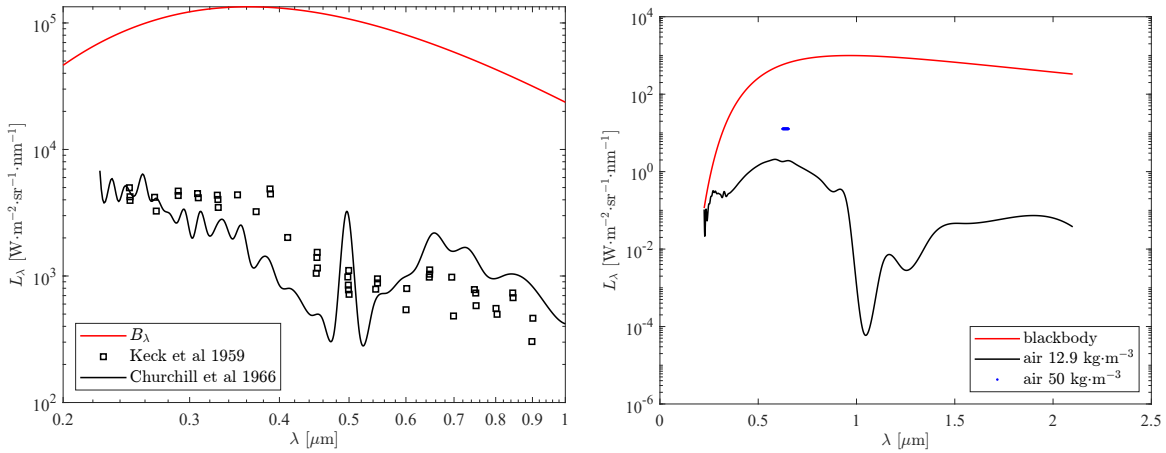

(a) (b)

Figure 21: (a) Spectral radiance of equilibrium air at 8000 K and 1 kg·m^{-3}, data from Keck et al. (1959) compared to model of Churchill et al. (1966) for 1.293 kg·m^{-3}. (b) Spectral radiance of equilibrium air at 3000 K and 12.93 kg·m^{-3} based on model of Churchill et al. (1966) with a depth of 4 mm. Planck black body spectral radiance is shown for reference for both cases.

$= \sin^{-1}(r/R)$. The imaging system collects light through an area of

$$A_c = 2\pi R^2(1-\cos\theta_0) = 4\pi R^2 \sin^2\frac{\theta_0}{2} \tag{34}$$

For $R >> r$ or equivalently $\theta_0 << 1$, the collection area is approximately $\pi R^2\theta_0^2 \simeq \pi r^2$ and the solid angle of collection is

$$\Omega_o \equiv \frac{A_c}{R^2} \simeq \pi\frac{r^2}{R^2}, \tag{35}$$

The area being imaged is related to the area of the sensor pixel through the magnification factor m of the imaging system

$$A_i = m^2 A_o. \tag{36}$$

Collecting all of the terms, the number of electrons collected by a sensor pixel per frame will be

$$N_{e^-} = \pi\frac{r^2}{R^2}\frac{A_i}{m^2}\eta\frac{\int_0^{t_{int}} L_o(t)\mathrm{d}t}{h\nu} \tag{37}$$

The digital signal output will be an integer I determined by the well depth (maximum number of electrons on the sensor element) $N_{e^-}^w$ and the number of maximum number of bits n in the digitizer output. Assuming an ideal sensor and processing electronics with a linear conversion of charge to voltage to bits, the resulting digital signal displayed as the sensor output by the software will be

$$V \propto 2^n\frac{N_{e^-}}{N_{e^-}^w} \tag{38}$$

with the constant of proportionality determined by the details of the photodiode and electronic circuitry. Well-designed sensors have a reasonably linear response up to saturation, which corresponds to the filling the charge well. The residual charge in the well and any noise will result in an offset from zero.

An estimate of the brightness of the luminous region in terms of number of electrons collected was made using this idealized model by evaluating (37) and the values of parameters in Table 2. The imaging system parameters were obtained from Dworzanczyk et al. and the sensor performance parameters are based on published data (Crooks et al., 2013b,a). The radiance was obtained from the extrapolated absorption coefficient, a 3000 K layer of 50 kg·m^3 shock heated layer with a depth of 4 mm filtered through the 640 $\pm$7 nm bandpass filter. The estimate is

$$\boxed{N_{e^-} = 166}$$

Table 2: Parameters in photon budget.

Imaging Optics		
L_o	178	W·m^{-2}·sr^{-1}
t_{int}	100	μs
R	2.8	m
r	62	mm
m	0.693	
$h\nu$	3.1×10^{-19}	J
Sensor Parameters		
A_i	9×10^{-10}	m^2
η	.023	
$N_{e^-}^{w}$	1.117×10^{4}	
$N_{e^-}^{rms}$	$<$10	
n	10	
fill factor	11%	
Number of Electrons Collected		
N_{e^-}	166	

Is this enough? In order to evaluate the visibility, we need to examine the raw data from the sensor, shown in Fig. 23, for the frame at 15.75 μs shown in Fig. 18c. The ghosting and image lag is apparent in comparion to the processed images (Fig. 17). The intensity histogram (Fig. 23b) indicates that only about 20% of the dynamic range of the sensor is being used.

The characteristic intensity profiles corresponding to the luminous region can be observed in Fig. 23c,d as in the enhanced images but the signal to noise ratio is much lower and there is a substantial offset due to uncorrect dark signal. The predicted luminosity signal of 166 electrons amounts to 1.4% of the well depth or a predicted digital signal of 14, about 16 times the rms noise The peak value of the digital signal at the brightest part of the luminosity is 120 (out of 1024) but there the dark signal correction is unknown and the pixels that have little or no illumination show a value of 32-50. The actual recorded signal therefore appears to be five times larger than the prediction. We conclude that the luminous region is not an artifact. The model for the optical and senor performance is primitive and the factor of five difference in measured and predicted radiance is not too surprising.

Much brighter images can be observed on the TMX7510 images and immediately after image, the location appears to coincide with the reflected bow shock region, forming a luminous disk around the impact point, Fig. 22. The magnification and frame rate were much lower than for the Kirana images so less detail can be observed although evidence of the drop and flyer bow shocks can be discerned. The sensor appears to be saturated by the emission due to impact, this may have resulted in 'blooming' of the image so the actual extent of the luminous region is unknown.

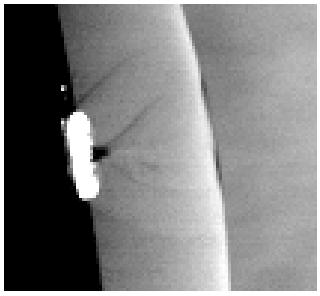

Figure 22: Luminosity recorded by TMX7510 immediately after impact for Drop 9. The image has been cropped and the contrast stretched.

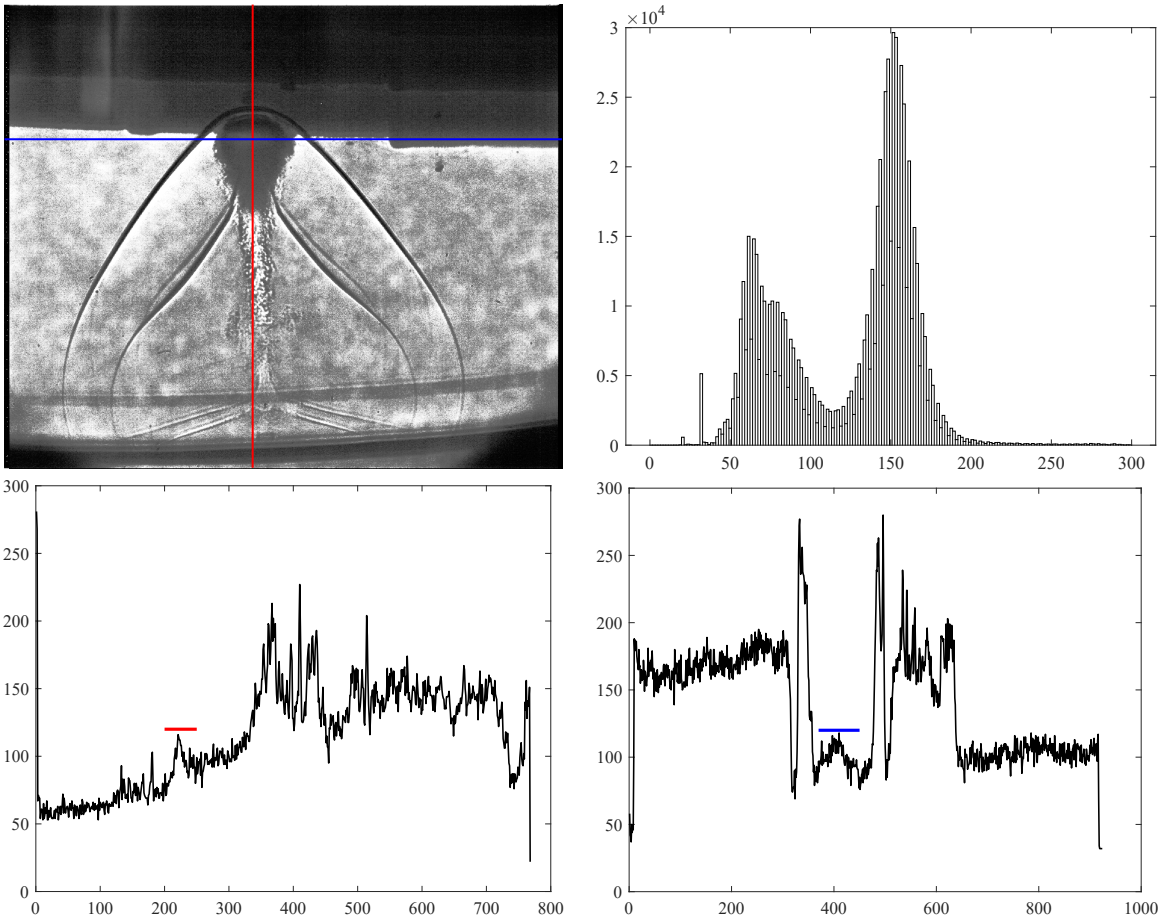

Figure 23: Raw data from Kirana camera processed from tiff files. a) Frame 92 at 15.75 μs. b) Histogram of gray scale values which range between 0-1024 but with very few values greater than 300. c) gray scale data along axis of impact. b) gray scale data perpendicular to impact axis and through center of bright region.

9 Conclusions

1. The temperature of shocked liquid water is too low to contribute to significant, narrow-band luminous emission in the visible wavelengths.
2. The temperature of the shocked air or air/water vapor mixture may be high enough to create sufficiently luminosity if we account for the reverberation of the drop bow shock during the impact event.
3. The possibility of optical artifacts as the source of the bright flashes should be ruled out through further testing.

Further work and unresolved issues

Some suggestions for optical diagnostics in future testing include:

1. Imaging

   Use baffles to attempt to avoid unwanted illumination from the launcher, a notch filter to block scattered light from the shadowgraph illumination laser, and low f-number optics to image the impact region with a short depth of focus. An additional high-speed CMOS camera at a slightly oblique angle to the shadowgraph optical axis could be used to record these images. The baffles could be as simple as cardboard tubes and sheets painted black. These will be destroyed and have to be replaced in each test and can be located just out side the flyer bow shock to survive long enough to be effective.

   Choice of camera: Although the Kirana has much higher spatial resolution, it is has lower sensitivity than either the Shimadzu HPV-X2 or Phantom TMX7510. The advantage of the Shimadzu is much higher frame rate but at the cost of lower resolution than the Kirana but higher than the TMX. The TMX 7510 has a much lower maximum framing rate and limited resolution but is much more sensitive than either the Kirana or HPV-X2, the quoted quantum efficiency is 78% and extends down to 300 nm, the pixel size is 18.5 μm with an almost 100% fill fact, and the ADC has 12-bit resolution. The minimum exposure time of 100 ns is comparable for the Kirana and HPV-X2, the exposure time for the TMX 7510 can be even shorter. The Kirana has a number issues with artifacts, ghosting and image lag, particularly at low light levels.

2. Spectroscopy

   The spectral signatures of shocked air and water will be sufficiently different that some insight could be gained by time revolved and spectrally-resolved measurements. A spectrometer or bandpass filters in front of fast photo detectors could be used to do the spectral separation. High-speed linear arrays at the image plane of a spectrometer could be used to resolve a portion of the spectrum along a segment of the impact axis. It will be necessary to use a high-speed intensified camera coupled to the grating spectrometer, similar to the arrangement used by Yanes (2020) with modifications to examine a wider range of wavelengths in the visible and near UV (300-800 nm). It will be necessary to use an imaging system based on a reflecting telescope if UV-transmitting lenses are not available.

   Hot water has very distinctive band emission in the mid-IR whereas prominent features of shocked air involve line spectra from atomic transitions and recombination. Dissociated water produces excited OH molecules which has a distinctive band in the 300-340 nm range. There is a long history of spectroscopic measurements behind shock waves and a number of potential pitfalls such as strong lines from metals and contaminants. However, on the whole, spectroscopic measurements could provide valuable insight into the impact processes.

3. Improve estimates of the emission by using HiTRAN or HiTEMP.

Other factors to consider in analyses

1. Wave interactions following impact

   Immediately following the impact, shock waves will propagate forward into the flyer and backward into the water drop and surrounding mist. These wave will reflect from the surfaces opposite the impact point and produce expansion waves. These waves can produce spallation (solid) or cavitation (liquid) which can create addition sources of luminosity. These event will happen within the time frame for wave propagation through the flyer and drop, 2-3 μs.

2. Mixing of air and water

   The drop is surrounded by water mist stripped from the drop following penetration through the flyer bow shock. This mist will mix with air and alter the postshock state behind the drop bow shock as well as the state following drop bow shock reflection from flyer. This will alter the thermodynamic state and the optical emission properties of shocked layer.

3. Drop leading edge shape

   The images from Dworzanczyk et al. show a corrugated drop surface prior to impact. These corrugations could create trapped pockets of gas that are compressed to a higher extent than the reflected bow shock wave. A speculative consequence is that a bubble-like region is created that is imploded during and following impact.

4. Bubble collapse luminescence

   Trapped gas pockets or cavitation bubbles (Brennen, 1995) created by expansion waves may collapse due to compression following the impact event; these are possible sources of luminosity. There has been extensive (Crum, 2015) research on light emission from cavitation produced by oscillating bubbles created by high-intensity ultrasonic fields in liquids, particularly the phenomenon of single bubble sonoluminescence (SBSL) (Brenner, 2002). The light emission from SBSL is created when a small (less than 10 μ radius) bubble is trapped in an acoustic field for thousands of cycles. The bubble oscillations and imposed acoustic field are in resonance, resulting in highly nonlinear oscillations of the bubble size culminating in a rapid collapse to an exceptionally small dimension; light emission occurs at this point. The light pulses are visible to the eye although dim. The characteristic width is 50-500 ps and the number of photons emitted per pulse ranging from 10^4 (Didenko and Suslick, 2002) to 10^7 Barber et al. (1997), although significant variations are observed depending on the amount and type of dissolved gas, bubble size, amplitude and frequency of the ultrasonic acoustic field (Barber et al., 1997).

   The mechanism of emission of light has long been controversial (Brenner, 2002), with the most accepted explanation being the most prosaic: adiabatic heating of the gas inside the bubble with the potential for shock formation Moss et al. (1999) although the temperature profile within the gas may prevent compression wave steepening Vuong et al. (1999). A wide range of peak temperatures (7,000-20,000 K) have been estimated and chemical reactions, particularly in water vapor, have been considered Storey and Szeri (2000), Yasui (2021) and are expected to limit the peak temperatures and brightness of the water emission.

   More relevant to the present study is a single bubble formation and collapse cycle produce by a pressure transient. Less data is available on these events, one example is the emission from laser-induced bubbles by Baghdassarian et al. (1999). They observed longer light pulses (5-10 ns) with up to 10^8 photons per flash (integration over 300-600 nm wavelength) depending on the maximum bubble radius, which were 400-800 μm, orders of magnitude larger than SBSL. Spectroscopic observations of multibubble sonoluminescence byFlint and Suslick (1991) in silicone oil were consistent with Swan band emission of C_2 molecules at an effective temperature of 5000 K.

   Clearly, emission from bubble collapse is a potential source of luminosity. Further investigation is needed to determine if a credible case can be made for observable luminosity from the generation and collapse of bubbles on the times scales observed in the present experiments.

5. Improved equations of state for both the compressed water and the air-water gas mixtures will be needed to make quantitative estimates of shocked states in numerical simulations. A more challenging issue is the modeling of mixed phase states.

Acknowledgment

Thanks Nick, for giving me a fun challenge and the raw material. Thanks to Dr. Abreau and the surgical team at Keck Norris Cancer Hospital for their care. My successful recovery at home enabled me to focus on this project. I don't recommend a significant "life event" as inspiration for scholarly activity although this is the second time[5] in seven years I have done so!

[5]The first is documented in Optics of the Human Eye and Intraocular Gas

References

SESAME: The Los Alamos National Laboratory Equation of State Database. Technical Report LA-UR-92-3407, Los Alamos National Laboratory, Los Alamos, NM, 1992. 12

B.H. Armstrong, D R Churchill, and K. G. Mueller. Absorption Coefficients of Heated Air: A Compilation to 24,000 K. Technical Report AFWL_TR 65-132, Vol. II, Air Force Weapons Laboratory, Kirtland Air Force Base, New Mexico, October 1965. 18, 19, 20

Ohan Baghdassarian, Bernd Tabbert, and Gary A. Williams. Luminescence Characteristics of Laser-Induced Bubbles in Water. *Physical Review Letters*, 83(12):2437–2440, September 1999. 25

Bradley P. Barber, Robert A. Hiller, Ritva Löfstedt, Seth J. Putterman, and Keith R. Weninger. Defining the unknowns of sonoluminescence. *Physics Reports*, 281(2):65–143, March 1997. 25

S. A. Bordzilovskii, S. M. Karakhanov, and K. V. Khishchenko. Brightness temperature of water compressed by a double shock to pressures of 60–79 GPa. *Shock Waves*, 30(5):505–511, July 2020. 4, 7, 31

CE Brennen. *Cavitation and Bubble Dynamics*. Oxford University Press, 1995. 25

Michael P Brenner. Single-bubble sonoluminescence. *Rev. Mod. Phys.*, 74(2), 2002. 25

D R Churchill, B.H. Armstrong, R.R Johnston, and K.G. Muller. Absorption Coefficients of Heated Air: A Tabulation to 24 000 K. *J. Quantitative Spectroscopy and Radiative Transfer*, 6:371–442, 1966. 18, 19, 21

J P Cocchi, R Saurel, and J C Loraud. Treatment of interface problems with Godunov-type schemes. *Shock Waves*, 5 (6):347–357, 1996. 13, 35

A Coppalle and P Vervisch. Spectral emissivities of H_2O vapor at 2900 K in the 1-9-μm region. *Journal of Quantitative Spectroscopy and Radiative Transfer*, 35(2):121–125, 1986. 18

M. Cowperthwaite and R. Shaw. $C_v(T)$ equation of state for liquids. calculation of the shock temperature of carbon tetrachloride, nitromethane, and water in the 100-kbar region. *The Journal of Chemical Physics*, 53(2):555–560, July 1970. 7, 30, 32, 33

J Crooks, B Marsh, R Turchetta, K Taylor, W Chan, A Lahav, and A Fenigstein. Ultra-high speed imaging at megaframes per second with a megapixel CMOS image sensor. In *Intl. Image Sensor Workshop*, Snowbird, Utah, USA, 2013a. 19, 21

J. Crooks, B. Marsh, R. Turchetta, K. Taylor, W. Chan, A. Lahav, and Amos Fenigstein. Kirana: A solid-state megapixel uCMOS image sensor for ultrahigh speed imaging. In Ralf Widenhorn and Antoine Dupret, editors, *IS&T/SPIE Electronic Imaging*, page 865903, Burlingame, California, USA, February 2013b. 21

Lawrence A Crum. Sonoluminescence. *Physics Today*, 47:22–29, September 1994. 1

Lawrence A. Crum. Resource Paper: Sonoluminescence. *The Journal of the Acoustical Society of America*, 138(4): 2181–2205, October 2015. 25

Yuri T. Didenko and Kenneth S. Suslick. The energy efficiency of formation of photons, radicals and ions during single-bubble cavitation. *Nature*, 418(6896):394–397, July 2002. 25

A.R. Dworzanczyk, M. Viqueira-Moreira, J.D. Langhorn, M.A. Libeau, C. Brehm, and N.J. Parziale. On aerobreakup in the stagnation region of high-Mach-number flow over a bluff body. *Journal of Fluid Mechanics*, 1002:A1, January 2025. 1, 4, 12, 13, 14, 16, 17, 18, 21, 25

EDL. Shock and Detonation Toolbox. California Institute of Technology, March 2019. 13

Edward B. Flint and Kenneth S. Suslick. The Temperature of Cavitation. *Science*, 253(5026):1397–1399, September 1991. 25

Kazuhisa Fujita, Sunichi Sato, Takashi Abe, and Yuta Ebinuma. Experimental Investigation of Air Radiation from Behind a Strong Shock Wave. *Journal of Thermophysics and Heat Transfer*, 16(1):77–82, January 2002. 18

A. G. Gaydon and I. R. Hurle. *The Shock Tube in High-Temperature Chemical Physics*. Chapman and Hall, 1963. 1, 18

David G. Goodwin, Harry K. Moffat, and Raymond L. Speth. Cantera: An Object-oriented Software Toolkit for Chemical Kinetics, Thermodynamics, and Transport Processes, 2017. 8, 13

G. A. Gurtman, J. W. Kirsch, and C. R. Hastings. Analytical Equation of State for Water Compressed to 300 Kbar. *Journal of Applied Physics*, 42(2):851–857, February 1971. 7

Peter Hallstadius. Development of an analytical exponential-6 equation of state through Monte Carlo simulations. *The Journal of Chemical Physics*, 159(16):164501, October 2023. 32

F. Harlow and A.A. Amsden. Fluid Dynamics. Technical Report LA-4700, Los Alamos Scientific Laboratory, Los Alamos, NM, June 1971. 13

Allan H. Harvey, Jan Hrubý, and Karsten Meier. Improved and Always Improving: Reference Formulations for Thermophysical Properties of Water. *Journal of Physical and Chemical Reference Data*, 52(1):011501, March 2023. 31

R. Jeanloz, P. M. Celliers, G. W. Collins, J. H. Eggert, Kanani K. M. Lee, R. Stewart McWilliams, Stéphanie Brygoo, and Paul Loubeyre. Achieving high-density states through shock-wave loading of precompressed samples. *Proceedings of the National Academy of Sciences*, 104(22):9172–9177, May 2007. 4

Eric Johnsen and Tim Colonius. Shock-induced collapse of a gas bubble in shockwave lithotripsy. *The Journal of the Acoustical Society of America*, 124(4):2011–2020, October 2008. 13

James C. Keck, J.C. Camm, B. Kivel, and T Wentink. Radiation from Hot Air. Part II. Shock Tube Study of Absolute Intensities. *Annals of Physics*, 7:1–38, 1959. 1, 18, 19, 21

J.H. Keenan, F.G. Keyes, P.C. Hill, and J.G. Moore. *Steam Tables : Thermodynamic Propertis of Water Incluiding Vapor, Liquid, and Solid Phases*. John Wiley and Sons, Inc., New York, 1969. 9, 31

S.B. Kormer. Optical Study of the Characteristics of Shock-Compressed Condensed Dielectrics. *Soviet Physics Uspekhi*, 11(2):229–254, 1968. 4, 7, 30

C. B. Ludwig. Measurements of the Curves-of-Growth of Hot Water Vapor. *Applied Optics*, 10(5):1057, May 1971. 18

G. A. Lyzenga, Thomas J. Ahrens, W. J. Nellis, and A. C. Mitchell. The temperature of shock-compressed water. *The Journal of Chemical Physics*, 76(12):6282–6286, June 1982. 4, 7, 30

S. P. Marsh. *LASL Shock Hugoniot Data*. University of California Press, 1980. 3, 6

B. J. McBride, M. J. Zehe, and S. Gordon. NASA Glenn Coefficients for Calculating Thermodynamic Properties of Individual Species. Technical Paper 2002-211556, NASA, 2002. 8, 13

Marius Millot, Sebastien Hamel, J. Ryan Rygg, Peter M. Celliers, Gilbert W. Collins, Federica Coppari, Dayne E. Fratanduono, Raymond Jeanloz, Damian C. Swift, and Jon H. Eggert. Experimental evidence for superionic water ice using shock compression. *Nature Physics*, 14(3):297–302, March 2018. 4

A. C. Mitchell and W. J. Nellis. Equation of state and electrical conductivity of water and ammonia shocked to the 100 GPa (1 Mbar) pressure range. *The Journal of Chemical Physics*, 76(12):6273–6281, June 1982. 4

William C. Moss, David A. Young, Judith A. Harte, Joanne L. Levatin, Balazs F. Rozsnyai, George B. Zimmerman, and I. Harold Zimmerman. Computed optical emissions from a sonoluminescing bubble. *Physical Review E*, 59(3): 2986–2992, March 1999. 25

K. Nagayama, Y. Mori, K. Shimada, and M. Nakahara. Shock Hugoniot compression curve for water up to 1 GPa by using a compressed gas gun. *Journal of Applied Physics*, 91(1):476, 2002. 4

V. Parekh, D. Gildfind, S. Lewis, and C. James. X3 expansion tube driver gas spectroscopy and temperature measurements. *Shock Waves*, 28(4):851–862, July 2018. 18

T. E. Parker, M. F. Miller, K. R. McManus, M. G. Allen, and W. T. Rawlins. Infrared emission from high-temperature $H_2O(\nu_2)$ - a diagnostic for concentration and temperature. *AIAA Journal*, 34(3):500–507, March 1996. 18

XiaoJuan Peng, FuSheng Liu, ShiLai Zhang, MingJian Zhang, and FuQian Jing. The C_υ for calculating the shock temperatures of water below 80 GPa. *Science China Physics, Mechanics and Astronomy*, 54(8):1443–1446, August 2011. 7, 30

W. C. Reynolds. *Thermodynamic Properties in SI: Graphs, Tables, and Computational Equations for Forty Substances*. Dept Mechanical Engineering, Stanford University, 1979. 9

M. H. Rice and J. M. Walsh. Equation of State of Water to 250 Kilobars. *The Journal of Chemical Physics*, 26(4): 824–830, April 1957. 4, 7, 10, 30

L.S. Rothman, I.E. Gordon, R.J. Barber, H. Dothe, R.R. Gamache, A. Goldman, V.I. Perevalov, S.A. Tashkun, and J. Tennyson. HITEMP, the high-temperature molecular spectroscopic database. *Journal of Quantitative Spectroscopy and Radiative Transfer*, 111(15):2139–2150, October 2010. 18

A. Saul and W. Wagner. A Fundamental Equation for Water Covering the Range from the Melting Line to 1273 K at Pressures up to 25 000 MPa. *Journal of Physical and Chemical Reference Data*, 18(4):1537–1564, October 1989. 31, 32

J. E. Shepherd. Interface effects in underwater explosions. In *Conventional Weapons Underwater Explosions*, pages 43–83, Atlanta, GA, December 1988. Office of Naval Research. 5, 7, 32, 33

D.J. Steinberg. Spherical explosions and the equation of state of water. Technical Report UCID-20974, 6766676, Lawrence Livermore National Laboratory, Livermore CA, February 1987. 3, 5, 6

Brian D. Storey and Andrew J. Szeri. Water vapour, sonoluminescence and sonochemistry. *Proceedings of the Royal Society of London. Series A: Mathematical, Physical and Engineering Sciences*, 456(1999):1685–1709, July 2000. 25

J.C. Tannehill and P.H. Mugge. Improved Curve Fits for the Thermodynamic Properties of Equilibrium Air Suitable for Numerical Computation Using Time-Dependent or Shock-Capturing Methods. Contractor Report CR-2470, NASA, 1974. 12

K.J. Taylor and P.D. Jarman. The Spectra of Sonoluminescence. *Aust. J. Phys.*, 23:319–34, 1970. 1

PA Thompson. An Equation for liquid-vapor saturation densities as a function of pressure. In *Equations of State in Engineering and Research*, volume 182, pages 365–383. American Chemical Society, 1978. 11

Vi Q. Vuong, Andrew J. Szeri, and David A. Young. Shock formation within sonoluminescence bubbles. *Physics of Fluids*, 11(1):10–17, January 1999. 25

W. Wagner and A. Pruß. The IAPWS Formulation 1995 for the Thermodynamic Properties of Ordinary Water Substance for General and Scientific Use. *Journal of Physical and Chemical Reference Data*, 31(2):387–535, June 2002. 11, 31, 32, 33

J. M. Walsh and R. H. Christian. Equation of State of Metals from Shock Wave Measurements. *Physical Review*, 97 (6):1544–1556, March 1955. 2, 3, 7

J. M. Walsh and M. H. Rice. Dynamic Compression of Liquids from Measurements on Strong Shock Waves. *The Journal of Chemical Physics*, 26(4):815–823, April 1957. 4, 7

R.W. Woolfolk, M. Cowperthwaite, and R. Shaw. A "universal" Hugoniot for liquids. *Thermochimica Acta*, 5(4): 409–414, February 1973. 3, 13

Nelson Javier Yanes. *Ultraviolet Radiation of Hypervelocity Stagnation Flows and Shock/Boundary-Layer Interactions*. PhD thesis, California Institute of Technology, Pasadena, CA (USA), 2020. 24

Kyuichi Yasui. Numerical simulations for sonochemistry. *Ultrasonics Sonochemistry*, 78:105728, October 2021. 25

Ya. B. Zel'dovich and Yu. P. Raizer. *Physics of Shock Waves and High-Temperature Hydrodynamic Phenomena*, volume 1 and 2. Wiley, NY, 1966. 1, 18

A Shocked Liquid Water Temperature Measurements

Key experimental and computations results from previous studies are reproduced in this Appendix. The experimental studies were all carried out with either high explosive or gas gun impact shock wave propagation.

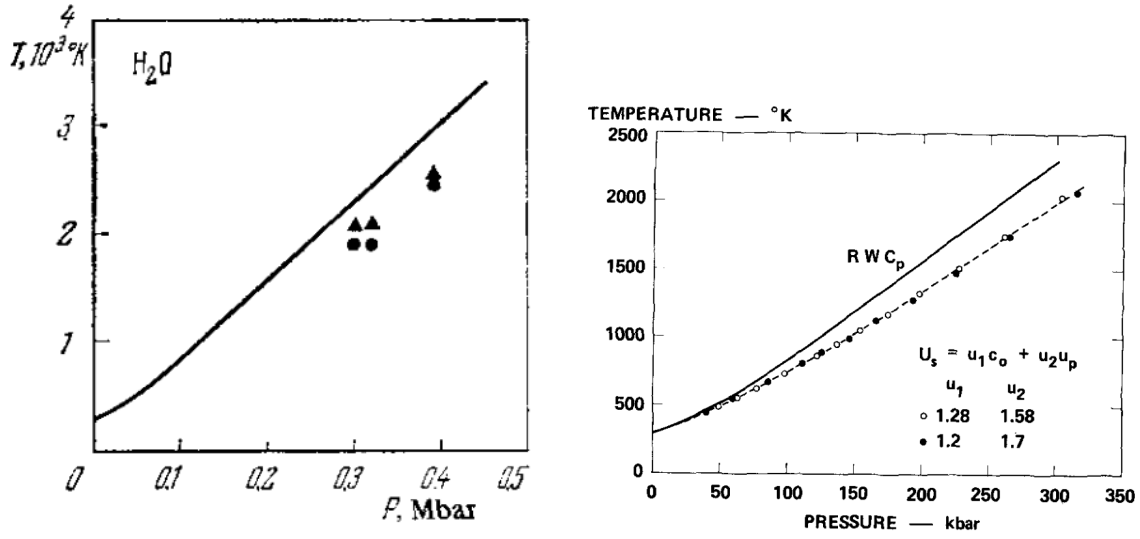

(a) (b)

Figure 24: (a) Figure 21 of Kormer (1968). (b) Figure 5 of Cowperthwaite and Shaw (1970) comparing the original Rice and Walsh (RW) estimates to their revised values.

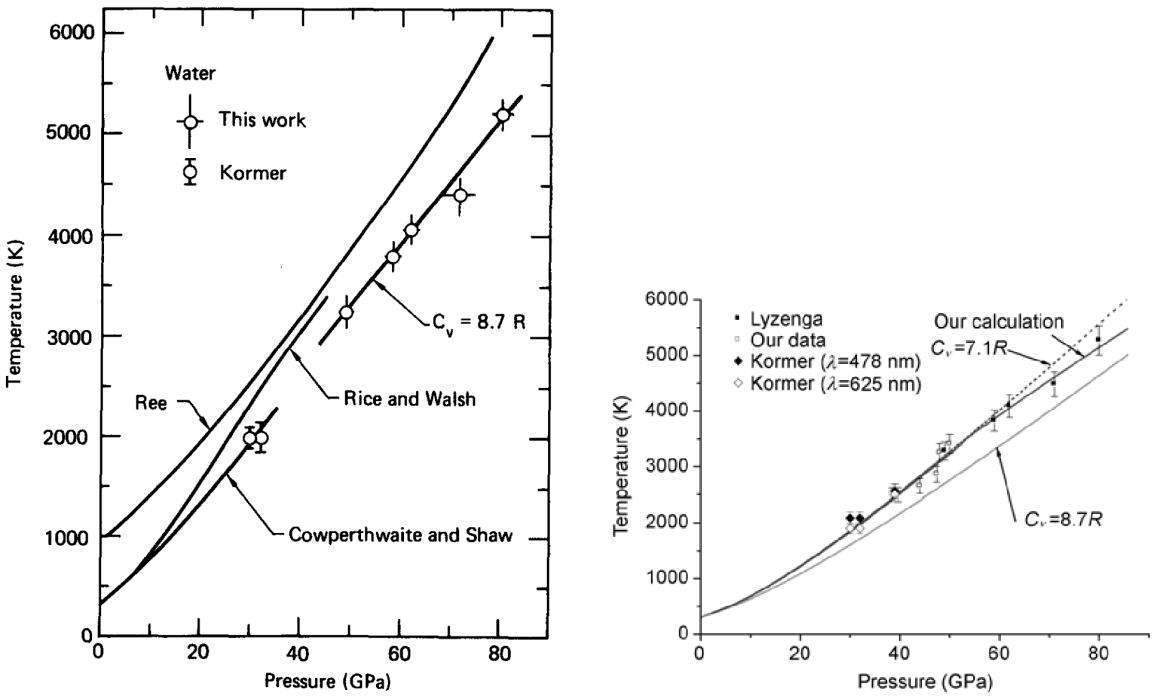

(a) (b)

Figure 25: (a) Figure 5 of Lyzenga et al. (1982). (b) Figure 4 of Peng et al. (2011).

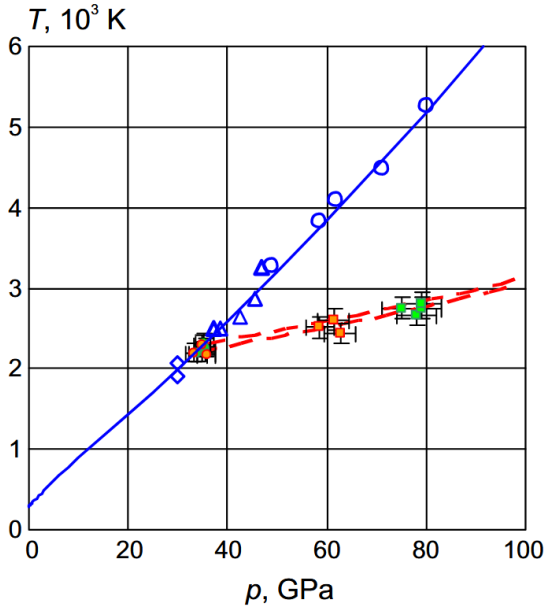

Figure 26: Figure 8 of Bordzilovskii et al. (2020). The data associated with the red dashed trend lines is from reflected shock waves into a shocked initial state indicated by the intersection with the incident shock wave speed curve.

B Water Equation of State

In order to form a complete and consistent equation of state, the thermodynamic potential must be expressed as a function of the conjugate variables. For water the choice has been the Helmholtz energy $F(T, \upsilon)$ since this approach was adopted by Keenan et al. (1969). Recent implementations include those of Saul and Wagner (1989), Wagner and Pruß (2002). The approach is to use fundamental thermodynamic relationships to compute all other properties. Starting with the fundamental relation of thermodynamics

$$\mathrm{d}F = -S\mathrm{d}T - P\mathrm{d}\upsilon \tag{39}$$

to define the pressure and entropy

$$P = -\left(\frac{\partial F}{\partial \upsilon}\right)_T \tag{40}$$

$$S = -\left(\frac{\partial F}{\partial T}\right)_\upsilon \tag{41}$$

and the internal energy is defined as

$$E = F - TS. \tag{42}$$

Heat capacity is determined from the definition

$$C_\upsilon = \left(\frac{\partial E}{\partial T}\right)_\upsilon = T\left(\frac{\partial S}{\partial T}\right)_\upsilon, \tag{43}$$

$$= -T\left(\frac{\partial^2 F}{\partial T^2}\right)_\upsilon. \tag{44}$$

The computation of F is usually partitioned into two steps Harvey et al. (2023). The ideal gas function F^{ig} is computed as a function of temperature and volume using statistical thermodynamics and the spectroscopic data. The departure or residual function $F^r = F - F^{ig}$ is evaluated using various methods that take into account the intermolecular

interactions for the dense gas, supercritical fluid. and liquid states. Special approaches are required for high pressure and density states encountered in strong shocks in liquid or condensed detonations, Hallstadius (2023). The main challenge in using these equations of state for the shocks in water with $1 < P < 10$ GPa is the lack of experimental data. The $U_s(u_p)$ measurements have a large gap in range and these only provide limited information in the vicinity of the shock adiabat. Despite this limitation is the useful to examine the results of computations with the most recent internationally accepted equation of state for water, IAPWS 1995, (Wagner and Pruß, 2002). Evaluation of the NIST implementation along isotherms and isobars was used to compute the graphs shown in the following figures.

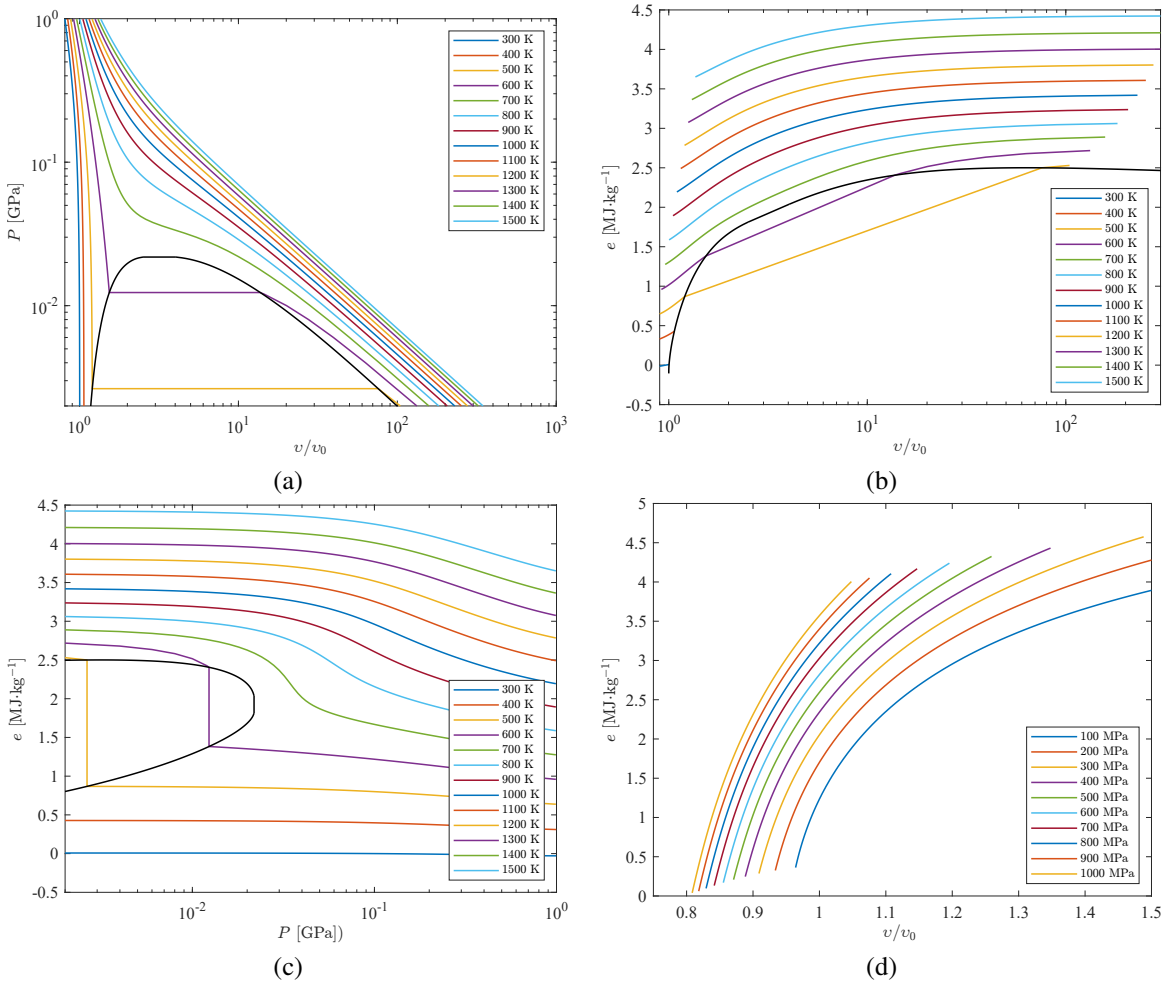

Figure 27: Thermodynamic states of water relevant to shock compression and release states for $P < 1$ GPa. Data from NIST based on Wagner and Pruß (2002).

It is instructive to examine the locus of shock states in the T-S representation (Fig. 28a) and on the surface $e(P, \upsilon)$ (28b). There is overlap between the shock adiabat and the isotherms in the interval $0 < P < 1$ GPa. The shock locus lies on or close to the EOS surface in a very restricted range. The temperature increase in a 1 GPA shock is approximately 30-40 K. The estimates of shock temperature in §5 using a constant specific heat compared with the NIST results in Fig. 29. The results of Cowperthwaite and Shaw are within 1 K of the NIST results at the same shock pressure while the results of Shepherd are 15 K higher. These differences are due to the different choices of specific heat capacity and Grüneisen coefficient in the two models. To extend this comparison to stronger shocks, the computations will need to use an equation of state such as proposed by Saul and Wagner (1989) or Hallstadius. Finally, from Fig. 28a, we note that the decompression of the shocked stated to ambient pressure will occur primarily along isentropes (vertical lines). This is will result in states within the two-phase region and following equilibrium, knowledge of the entropy s and P will enable prediction of the final vapor volume fraction and mixture temperature.

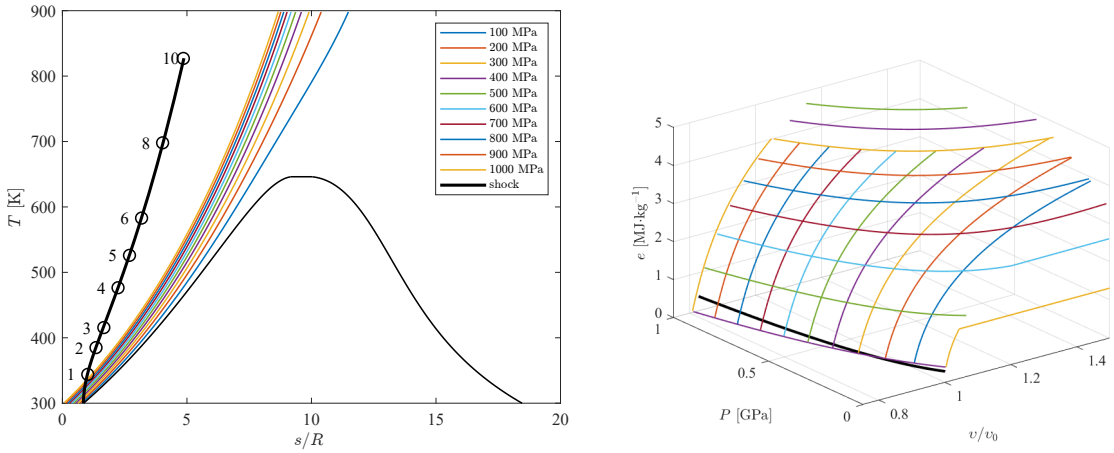

(a) (b)

Figure 28: Thermodynamic states of water relevant to shock compression and release states for $P < 1$ GPa. Data from NIST based on Wagner and Pruß (2002).

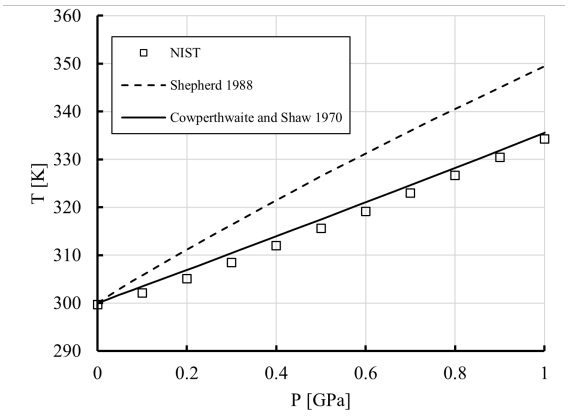

Figure 29: Comparison of temperatures computed by Shepherd and Cowperthwaite and Shaw with the results of evaluating the NIST data (Wagner and Pruß, 2002) on the shock adiabat.

C Shock waves in a Stiffened Gas

Consider the stiffened gas equation of state (EOS) in the form

$$P = (n-1)\rho e - nP_\infty \tag{45}$$

using the symbol n instead of γ to avoid any confusion with the standard nomenclature. We can combine the EOS with the shock jump conditions to obtain an explicit expression for $U_s(u_p)$. First, eliminate the constant P_∞ by rewriting the EOS in term of the initial states $()_1$

$$P - P_1 = \frac{\rho}{\rho_1}\left[e - e_1 + \left(1 - \frac{\rho}{\rho_1}\right)e_1\right]. \tag{46}$$

Solving for internal energy explicitly this can be written as

$$e - e_1 = \frac{P - P_1}{(n-1)\rho_1}\frac{\rho_1}{\rho} - \left(1 - \frac{\rho}{\rho_1}\right)e_1. \tag{47}$$

Now equate this to the energy jump across as a shock wave (3)

$$e - e_1 = -\frac{u_p^2}{2} + \frac{P}{\rho_1}\left(1 - \frac{\rho}{\rho_1}\right). \tag{48}$$

and simplify using (1) to eliminate density

$$1 - \frac{\rho_1}{\rho} = \frac{u_p}{U_s} \tag{49}$$

and (13) to eliminate pressure in favor the velocity ratio u_p/U_s. The result is a quadratic equation in shock speed

$$U_s^2 - \frac{n+1}{2}u_p U_s - (n-1)\left(e_1 + \frac{P_1}{\rho_1}\right) = 0 \tag{50}$$

The constant term is equal to the speed of sound. To compute sound speed from an equation of state $e(P, v)$, we start with the definition of sound speed

$$a^2 = -v^2\left(\frac{\partial P}{\partial v}\right)_s , \tag{51}$$

and use the FRT in the form

$$T\mathrm{d}s = \mathrm{d}e + P\mathrm{d}v \, . \tag{52}$$

On the isentrope, this implies

$$\mathrm{d}e = P\mathrm{d}v \, . \tag{53}$$

From the equation of state, we have

$$\mathrm{d}e = \left(\frac{\partial e}{\partial v}\right)_P \mathrm{d}P + \left(\frac{\partial e}{\partial P}\right)_v \mathrm{d}v \, , \tag{54}$$

equating the last two expressions yields

$$\left(\frac{\partial P}{\partial v}\right)_s = -\frac{\left(\frac{\partial e}{\partial v}\right)_P + P}{\left(\frac{\partial e}{\partial P}\right)_v} , \tag{55}$$

or

$$a^2 = v^2 \frac{\left(\frac{\partial e}{\partial v}\right)_P + P}{\left(\frac{\partial e}{\partial P}\right)_v} \,. \tag{56}$$

For the stiffened gas equation of state, this is

$$a^2 = v\left[(n-1)\frac{e_1}{v_1} + nP - P_1\right] \tag{57}$$

The value at the initial state is

$$a_1^2 = (n-1)\left[e_1 + P_1 v_1\right] \tag{58}$$

Substituting in (50), we obtain the $U_s(u_p)$ relation

$$\boxed{U_s = \frac{n+1}{4}u_p + \sqrt{\left(\frac{n+1}{4}u_p\right)^2 + a_1^2}} \tag{59}$$

This is given (without derivation) in Cocchi et al. (1996). For weak shocks, $u_p/a_1 \ll 1$, we can expand the surd to obtain the approximate relation

$$U_s = a_1 + \frac{n+1}{4}u_p + \frac{1}{2}\left(\frac{n+1}{4}\frac{u_p}{a_o}\right)^2 + \ldots \,. \tag{60}$$

The slope of the relationship near the origin is

$$\frac{\partial U_s}{\partial u_p} = \frac{n+1}{4} \approx 2 \tag{61}$$

for typical values of $n \simeq 7$ used for the stiffened gas equation of state. This is consistent with the extrapolated impact data which has a slope of 1.89. The stiffened gas $U_s(u_p)$ relation will be tangent to the shock impact relationship for weak waves but increasing departs from the nearly linear relationship observed for $u_p \geq 0.5$ km·s^{-1}.

The constant P_∞ is fixed by evaluating (45) at the initial condition and using the initial sound speed (58) to obtain

$$p_\infty = \frac{\rho_1 a_1^2}{n} + P_1 \approx \frac{\rho_1 a_1^2}{n}. \tag{62}$$